

*A model for the wind-driven current in the wavy oceanic surface layer: apparent friction velocity reduction and roughness length enhancement*

Article

Accepted Version

Teixeira, M. A. C. ORCID: <https://orcid.org/0000-0003-1205-3233> (2018) A model for the wind-driven current in the wavy oceanic surface layer: apparent friction velocity reduction and roughness length enhancement. *Journal of Physical Oceanography*, 48. pp. 2721-2736. ISSN 0022-3670 doi: <https://doi.org/10.1175/JPO-D-18-0086.1> Available at <https://centaur.reading.ac.uk/79612/>

It is advisable to refer to the publisher's version if you intend to cite from the work. See [Guidance on citing](#).

To link to this article DOI: <http://dx.doi.org/10.1175/JPO-D-18-0086.1>

Publisher: American Meteorological Society

All outputs in CentAUR are protected by Intellectual Property Rights law, including copyright law. Copyright and IPR is retained by the creators or other copyright holders. Terms and conditions for use of this material are defined in the [End User Agreement](#).

[www.reading.ac.uk/centaur](http://www.reading.ac.uk/centaur)

**CentAUR**

Central Archive at the University of Reading

Reading's research outputs online



# AMERICAN METEOROLOGICAL SOCIETY

*Journal of Physical Oceanography*

## **EARLY ONLINE RELEASE**

This is a preliminary PDF of the author-produced manuscript that has been peer-reviewed and accepted for publication. Since it is being posted so soon after acceptance, it has not yet been copyedited, formatted, or processed by AMS Publications. This preliminary version of the manuscript may be downloaded, distributed, and cited, but please be aware that there will be visual differences and possibly some content differences between this version and the final published version.

The DOI for this manuscript is doi: 10.1175/JPO-D-18-0086.1

The final published version of this manuscript will replace the preliminary version at the above DOI once it is available.

If you would like to cite this EOR in a separate work, please use the following full citation:

Teixeira, M., 2018: A model for the wind-driven current in the wavy oceanic surface layer: apparent friction velocity reduction and roughness length enhancement. *J. Phys. Oceanogr.* doi:10.1175/JPO-D-18-0086.1, in press.

© 2018 American Meteorological Society



1 **A model for the wind-driven current in the wavy oceanic surface layer:**  
2 **apparent friction velocity reduction and roughness length enhancement**

3 Miguel A. C. Teixeira\*

4 *Department of Meteorology, University of Reading, Reading, United Kingdom*

5 \*Corresponding author address: Department of Meteorology, University of Reading, Earley Gate,

6 PO Box 243, Reading RG6 6BB, United Kingdom.

7 E-mail: m.a.teixeira@reading.ac.uk

## ABSTRACT

8 A simple analytical model is developed for the current induced by the wind  
9 and modified by surface wind-waves in the oceanic surface layer, based on a  
10 first-order turbulence closure and including the effect of a vortex force repre-  
11 senting the Stokes drift of the waves. The shear stress is partitioned between  
12 a component due to shear in the current, which is reduced at low turbulent  
13 Langmuir number ( $La_t$ ), and a wave-induced component, which decays over  
14 a depth proportional to the dominant wavelength ( $\lambda_w$ ). The model reproduces  
15 the apparent reduction of the friction velocity and enhancement of the rough-  
16 ness length estimated from current profiles, detected in a number of studies.  
17 These effects are predicted to intensify as  $La_t$  decreases, and are entirely at-  
18 tributed to non-breaking surface waves. The current profile becomes flatter for  
19 low  $La_t$  owing to a smaller fraction of the total shear stress being supported  
20 by the current shear. Comparisons with the comprehensive dataset provided  
21 by the laboratory experiments of Cheung and Street show encouraging agree-  
22 ment, with the current speed normalized by the friction velocity decreasing as  
23  $La_t$  decreases and  $\lambda_w$  increases if the model is adjusted to reflect the effects  
24 of a full wave spectrum on the intensity and depth of penetration of the wave-  
25 induced stress. A version of the model where the shear stress decreases to zero  
26 over a depth consistent with the measurements accurately predicts the surface  
27 current speed. These results contribute towards developing physically-based  
28 momentum flux parameterizations for the wave-affected boundary layer in  
29 ocean circulation models.

## 30 **1. Introduction**

31 Flow coupling across the air-water interface in oceanic regions takes place within boundary lay-  
32 ers where various properties adjust, over a relatively small fraction of the depth of the atmosphere  
33 and ocean, between their values in the interior of each fluid. The atmospheric and oceanic sur-  
34 face layers are the sub-layers of these boundary layers located nearest to the air-water interface,  
35 occupying about 10% of their depth, which have a decisive importance in mediating the turbulent  
36 fluxes of momentum, heat and gases between the atmosphere and the ocean (Csanady 2004), and  
37 where these fluxes are approximately constant. Hereafter, ‘surface layer’ will always be used with  
38 this meaning, although the term is often adopted in an oceanographic context to denote the whole  
39 oceanic boundary layer.

40 Whereas the atmospheric surface layer over land has a no-slip bottom boundary condition ap-  
41 plied at the ground, the atmospheric and oceanic surface layers in ocean regions are characterized  
42 by continuity of velocity and stress at the mobile air-water interface that separates them. This, on  
43 the one hand, leads to the generation of a wind-induced current in the oceanic surface layer, and  
44 on the other hand allows the generation of surface waves at the air-water interface. Both of these  
45 aspects considerably complicate the physics of these surface layers, especially the oceanic one, as  
46 is widely recognized (Thorpe 2005) and will be further discussed here.

47 Nevertheless, the oceanic surface layer is still largely understood and modeled based on the  
48 transposition to the ocean of theories developed for the atmospheric surface layer over land, where  
49 the effects of surface waves are not represented (Kraus and Businger 1994). Deficiencies in this  
50 approach become apparent when one realizes that key parameters in surface layer theory, such as  
51 the friction velocity  $u_*$  and roughness length  $z_0$  are deemed to take values in the ocean that seem

52 to be inconsistent with the values of the shear stress and the geometric properties of the air-water  
53 interface, respectively.

54 Standard surface layer theory is based on Monin-Obukhov scaling, which in the limit of neutral  
55 stratification reduces to a theory for the logarithmic mean wind profile. In the ocean, or in un-  
56 derwater flows measured in the laboratory, such a theory has been applied, with varying degrees  
57 of success, to model the mean current induced by the wind. However, it has often been detected  
58 that the value of  $u_*$  inferred from the current profile is noticeably smaller than the one that would  
59 be expected from the total shear stress (McWilliams et al. 1997, Kudryavtsev et al. 2008, Teixeira  
60 and Belcher 2010), a phenomenon sometimes alternatively interpreted as an increase of the von  
61 Kármán parameter (Howe et al. 1982, Cheung and Street 1988, Craig and Banner 1994, Siddiqui  
62 and Loewen 2007). On the other hand, the value of  $z_0$  obtained by extrapolating the logarithmic  
63 current profile up to the surface is often much larger than would be expected based on the size of  
64 the surface corrugations deforming the air-water interface, and exceeds by several orders of mag-  
65 nitude the air-side value of  $z_0$  (Csanady 1984, Burchard 2001, Soloviev and Lukas 2003, Sullivan  
66 et al. 2004, Kudryavtsev et al. 2008).

67 There is some awareness that the first aspect is due to the fact that a fraction of the surface stress  
68 is carried by surface waves, and therefore does not support as much shear as if the waves were  
69 absent. On the other hand, the increased values of  $z_0$  have been attributed to the effect of surface  
70 waves as roughness elements seen from below, or to wave breaking, but the exact mechanism  
71 by which this enhancement arises remains rather mysterious. The huge disparity between the  
72 estimated values of  $z_0$  as seen from the air-side or from the water-side of the air-water interface is  
73 especially puzzling, since the amplitude of the corrugations is the same. Even if the flow on both  
74 sides of the air-water interface could be assumed to be aerodynamically smooth, the differences

75 in the value of  $u_*$  between air and water would not be enough to explain the magnitude of this  
76 disparity.

77 Craig and Banner (1994) and Craig (1996) developed a model of the oceanic surface layer that  
78 produces profiles of the mean current and of the associated dissipation rate of turbulent kinetic  
79 energy (TKE), which showed some success in predicting both quantities, and was subsequently  
80 adapted and used by a number of researchers (e.g., Drennan et al. 1996, Terray et al. 1999, Gemm-  
81 rich and Farmer 1999, Burchard 2001, Raschle et al. 2006, Feddersen et al. 2007, Raschle and Ard-  
82 huin 2009, Gerbi et al. 2009, Kukulka and Harcourt 2017). That model is based on an approximate  
83 balance between the turbulent fluxes of TKE and dissipation, and produces a substantial surface  
84 dissipation enhancement, which is consistent with the observations of Gargett (1989), Agrawal  
85 et al. (1992), Terray et al. (1996) and Drennan et al. (1996). However, it requires adjusting  $z_0$   
86 for each dataset, yielding values of this quantity of order the height or wavelength of the surface  
87 waves, which is much larger than estimated for an aerodynamically smooth boundary, or from  
88 the Charnock relation. Both Craig and Banner (1994) themselves and, more recently, Grant and  
89 Belcher (2009) recognized that this need to adjust  $z_0$  in order to fit measurements is a weakness of  
90 the model.

91 More recently, Kudryavtsev et al. (2008) developed a rather elaborate model based on the mo-  
92 mentum and TKE budgets, and assuming a balance between turbulence production by wave break-  
93 ing and dissipation. This model avoids the strong dependence on  $z_0$  displayed by the model of  
94 Craig and Banner (1994), but contains many *ad hoc* assumptions and approximations (for exam-  
95 ple, the parameterization of the TKE production by wave breaking, or the mixing length defi-  
96 nition), and nevertheless is so complicated that the corresponding equations can only be solved  
97 numerically. Although it predicts satisfactorily the qualitative behavior of the mean current pro-  
98 files measured in the laboratory experiments of Cheung and Street (1988) and the aforementioned



99 surface dissipation enhancement, it produces dissipation profiles that look somewhat artificial and  
100 seem to underestimate most datasets at small depths (see their Fig. 7). Although this model suc-  
101 ceeds in predicting the enhanced values of the apparent  $z_0$  in the experiments of Cheung and Street  
102 (1988), it does not explain the reduced values of  $u_*$  that can also be inferred from the slope of the  
103 mean flow profiles.

104 In this study a very simple model is developed, based on the partition of the shear stress in  
105 the surface layer between shear-related and wave-related parts, that reconciles all these results,  
106 explaining in particular the discrepancies between expected and observed values of  $u_*$  and  $z_0$  in  
107 the oceanic surface layer, purely due to the effect of non-breaking waves (unlike Kudryavtsev  
108 et al. 2008). The model draws heavily on that developed by Teixeira (2012), which is inspired  
109 by Rapid Distortion Theory (RDT) calculations, and is essentially analytical, being much simpler  
110 than the one proposed by Kudryavtsev et al. (2008), but is able to produce more accurate results.  
111 It has the advantage of being formulated as a variant of Monin-Obuhov scaling, where instead  
112 of the Obukhov stability parameter, the key dimensionless parameters account for the effects of  
113 surface waves. These parameters are the well-known turbulent Langmuir number  $La_t$  and (as  
114 in Monin-Obukhov theory) a dimensionless depth, here normalized by the wavenumber of the  
115 dominant surface waves. An extended version of this model was shown by Teixeira (2012) to give  
116 good predictions of the dissipation rate by comparison with field data from various sources (Terray  
117 et al. 1996, Drennan et al. 1996, Burchard 2001, Feddersen et al. 2007, Jones and Monismith 2008,  
118 Gerbi et al. 2009). The model is tested here by comparison with the data of Cheung and Street  
119 (1988), showing good agreement, despite the fact that (unlike the model of Kudryavtsev et al.  
120 (2008)) it uses a monochromatic wave approximation and neglects the viscous boundary layer.

121 This paper is organized as follows: section 2 presents the proposed model, including its version  
122 for a vertically uniform shear stress and its extension for a shear stress that decreases linearly with

123 depth. Section 3 contains the results, starting with tests to the model as a function of its input  
124 parameters, and proceeding with its comparison with laboratory data. Finally, in section 4, the  
125 main conclusions of this study are summarized.

## 126 **2. Theoretical Model**

127 It will be assumed that the rotation of the Earth and stratification of the water in the oceanic  
128 surface layer can be neglected. The first assumption is generally acceptable in the surface layer,  
129 where the flow is by definition dominated by turbulent fluxes (and throughout the whole oceanic  
130 boundary layer in Equatorial regions, where the Coriolis parameter is zero). The second assump-  
131 tion is acceptable if some other dynamical process (in the present case the effect of surface waves)  
132 is stronger than that of buoyancy. The effect of breaking surface waves will also be neglected.  
133 This is a working hypothesis, which is not as justifiable as the previous two, but was shown to be  
134 a plausible approximation given the level of agreement achieved between the model of Teixeira  
135 (2012) and dissipation data (for further details concerning its motivation, see that paper).

136 The water-side friction velocity  $u_*$  and roughness length  $z_0$  will be specified according to their  
137 most fundamental definitions: as the square-root of the surface value of the kinematic shear stress,  
138 and as the depth at which the current velocity relative to its surface value is zero (without assuming  
139 a displacement height), respectively, rather than based on the slope and intercept of the current  
140 profiles (which would be misleading in the present context).

141 The point of departure for the model is that turbulence in the surface layer is dominated by the  
142 transfer of kinetic energy from the mean wind-driven current and the Stokes drift of surface waves  
143 to the turbulence, via the shear production and Stokes drift production terms in the TKE budget  
144 (see, e.g., McWilliams et al. 1997), which are assumed to be balanced locally by the dissipation  
145 rate, as in Teixeira (2011b, 2012). This balance, although of questionable accuracy, has been

146 motivated in Teixeira (2012) by the TKE budgets presented in the Large Eddy Simulation (LES)  
 147 studies of Polton and Belcher (2007), Grant and Belcher (2009) and Kukulka et al. (2010) (which  
 148 did not account for the effects of wave breaking). More recent supporting evidence for this balance  
 149 is provided by Van Roekel et al. (2012) and Kukulka and Harcourt (2017).

150 RDT studies (e.g. Lee et al. 1990, Teixeira and Belcher 2002, Teixeira and Belcher 2010, Teix-  
 151 eira 2011a) have indicated that the characteristics of the turbulence (i.e., its anisotropy and rate  
 152 of energy transfer from the mean flow) are determined by its distortion by the mean current shear  
 153  $dU/dz$  (where  $U(z)$  is the mean current speed), which promotes horizontal ‘streaky structures’,  
 154 and by the Stokes drift gradient  $dU_S/dz$  (where  $U_S(z)$  is the Stokes drift velocity), which promotes  
 155 instead streamwise vortices with strong vertical velocity fluctuations. The influence of surface  
 156 waves can be measured by the relative importance of these two strain rates, since the correspond-  
 157 ing production terms in the TKE budget may be written (for a wind stress aligned in the  $x$  direction)

$$-\overline{u'w'}\frac{dU}{dz}, \quad -\overline{u'w'}\frac{dU_S}{dz}, \quad (1)$$

158 where  $\tau/\rho = -\overline{u'w'}$  is the kinematic shear stress (with  $u'$  and  $w'$  being the horizontal and vertical  
 159 turbulent velocity fluctuations, respectively) and  $\rho$  is the density. It will be assumed hereafter that  
 160  $dU/dz$  and  $dU_S/dz$  have the same sign ( $> 0$ ), which is the typical situation for wind-driven waves.

### 161 *a. Scaling of the oceanic surface layer*

162 The vertical gradient of the Stokes drift of a deep-water monochromatic surface wave of ampli-  
 163 tude  $a_w$ , wavenumber  $k_w$  and angular frequency  $\sigma_w$  at a depth  $z$  is given by (Phillips 1977)

$$\frac{dU_S}{dz} = 2(a_w k_w)^2 \sigma_w e^{-2k_w |z|}, \quad (2)$$

164 and, to a first approximation, in the surface layer the mean current shear satisfies

$$\frac{dU}{dz} = \frac{u_*}{\kappa |z|}, \quad (3)$$

165 where  $\kappa$  is the von Kármán constant. To evaluate the relative importance of the Stokes drift strain  
 166 rate and mean shear rate of the current, the ratio of (2) and (3) may be taken at a representative  
 167 depth where the flow is affected by surface waves, say  $|z| = 1/(2k_w)$ , yielding

$$R = \frac{dU_S/dz}{dU/dz}(|z| = 1/(2k_w)) = \kappa e^{-1} (a_w k_w)^2 \frac{c_w}{u_*} = \kappa e^{-1} \frac{U_S(z=0)}{u_*} = \kappa e^{-1} La_t^{-2}, \quad (4)$$

168 where  $U_S(z=0) = (a_w k_w)^2 c_w$  is the Stokes drift velocity at the surface,  $c_w = \sigma_w/k_w$  is the phase  
 169 speed of the waves, and  $La_t = (u_*/U_S(z=0))^{1/2}$  is the turbulent Langmuir number. Incidentally,  
 170  $|z| = 1/(2k_w)$  is also the depth at which  $R$  attains its maximum (cf. Teixeira and Belcher 2010,  
 171 Teixeira 2011a).

172 Consider first the magnitude of  $R$  in the atmosphere. Although one does not often think about  
 173 Stokes drift in the atmosphere, its magnitude is similar to that in the ocean, since the wave orbital  
 174 motions (usually immersed in a tangle of turbulent eddies) are likewise of similar magnitude.  
 175  $dU_S/dz$  is estimated here as if  $dU/dz$  did not affect the wave motion, which is certainly not strictly  
 176 true, but provides a leading-order approximation. For waves of slope  $a_w k_w \approx 0.1$  and wavelengths  
 177 in the range  $\lambda_w \approx 1 - 100$  m, taking into account that  $k_w = 2\pi/\lambda_w$ , then the wavenumber is in the  
 178 range  $k_w \approx 0.06 - 6.3 \text{ m}^{-1}$ , and using the linear dispersion relation of deep-water gravity waves,  
 179  $c_w = \sqrt{g/k_w}$ , one obtains  $c_w \approx 1.25 - 12.5 \text{ m s}^{-1}$ , with the limits swapped relative to those of  
 180  $k_w$ . Taking a typical value of the friction velocity in the atmosphere,  $u_* \approx 0.3 \text{ m s}^{-1}$ , (4) yields  
 181  $R \approx 6 \times 10^{-3} - 6 \times 10^{-2}$  (where  $\kappa = 0.4$  was assumed), which is very small. This means, perhaps  
 182 unsurprisingly, that the effect of the Stokes drift in the atmosphere is fairly insignificant, and the  
 183 surface layer should be dominated by mean wind shear.

184 For the oceanic surface layer, although the same estimates for the wave characteristics may be  
 185 used, it must be noted that, to a first approximation, the shear stress  $\tau$  is continuous across the  
 186 air-water interface in steady flow, and since by definition  $\overline{u'w'}(z=0) = -u_*^2$ , then  $\rho u_*^2$  must be

187 continuous at that interface. Given that the density ratio between water and air is  $\approx 833$ , the  
188 friction velocity in the water will be smaller by a factor of  $\sqrt{833} \approx 29$ . This gives a typical friction  
189 velocity of  $u_* \approx 0.01 \text{ ms}^{-1}$ , yielding  $R \approx 0.17 - 1.7$ , which is of  $O(1)$ . In reality, the value of  $u_*$   
190 used in (3) should be even smaller, since part of the shear stress is supported by the wave as well  
191 as by the mean shear (as will be seen later), so that it is common to have  $R$  substantially higher  
192 than 1. In addition, it is quite possible that  $a_w k_w > 0.1$ , which also increases  $R$ . This means that  
193 in the ocean it is unacceptable to ignore the effect of the Stokes drift of surface waves, and this  
194 difference is what gives oceanic turbulence its distinctive character, as shown by McWilliams et al.  
195 (1997) using LES and Teixeira and Belcher (2002, 2010) and Teixeira (2011a) using RDT.

### 196 *b. Shear stress partition*

197 The Craik-Leibovich equations including the effect of the Stokes drift of surface waves may be  
198 manipulated, in the same way as done for obtaining a TKE budget including the production terms  
199 (1), to obtain an equation for evolution of the shear stress (Teixeira 2011a):

$$\frac{d}{dt} \overline{u'w'} = -\overline{w'^2} \frac{dU}{dz} - \overline{u'^2} \frac{dU_S}{dz} + \text{other terms.} \quad (5)$$

200 This equation shows that the shear stress receives contributions proportional to the mean shear  
201 and to the Stokes drift strain rate. This prompted Teixeira (2011a) to decompose  $\overline{u'w'}$  into shear-  
202 induced and wave-induced components, proportional to the corresponding production terms ex-  
203 plicitly presented in (5). Hence, the shear-induced component of  $\overline{u'w'}$  can be parameterized as

$$(\overline{u'w'})_s = \overline{u'w'} \frac{\overline{w'^2} dU/dz}{\overline{w'^2} dU/dz + \overline{u'^2} dU_S/dz} = \frac{\overline{u'w'}}{1 + \frac{\overline{u'^2} dU_S/dz}{\overline{w'^2} dU/dz}} = \frac{\overline{u'w'}}{1 + \frac{\overline{u'^2}}{\overline{w'^2}} 2\kappa (a_w k_w)^2 \frac{c_w}{u_*} k_w |z| e^{-2k_w |z|}}, \quad (6)$$

204 where (2) and (3) have been used. Although the logarithmic current profile is modified by wave  
205 effects (as shown in the following section) and therefore (3) is not strictly accurate, it provides a  
206 correct scaling which makes the proposed shear stress partition both be simple enough and benefit

207 from good properties. The inaccuracy of this approximation is likely to partially cancel with those  
 208 of other adopted assumptions, as noted below. Using the definitions of  $u_*$ ,  $U_S(z=0)$  and  $La_t$ , (6)  
 209 may be alternatively expressed as

$$(\overline{u'w'})_s = -\frac{u_*^2}{1 + 2\kappa \frac{\overline{u'^2}}{w'^2} \frac{U_S(z=0)}{u_*} k_w |z| e^{-2k_w |z|}} = -\frac{u_*^2}{1 + 2\kappa \frac{\overline{u'^2}}{w'^2} La_t^{-2} k_w |z| e^{-2k_w |z|}}, \quad (7)$$

210 where it has been noted that in the surface layer the shear stress  $\overline{u'w'}$  is constant and equal to  $-u_*^2$ .  
 211 If, following Teixeira (2012), it is assumed that the quantity  $\gamma = 2\kappa(k_w |z|) \frac{\overline{u'^2}}{w'^2}$  is approximately  
 212 constant (which has some plausibility given that  $\overline{w'^2}$  must approach zero as  $z \rightarrow 0$ , particularly  
 213 in a curvilinear wave-following coordinate system – cf. Teixeira and Belcher (2002)), then the  
 214 shear-induced shear stress takes the form

$$(\overline{u'w'})_s = -\frac{u_*^2}{1 + \gamma La_t^{-2} e^{-2k_w |z|}}, \quad (8)$$

215 where  $\gamma$  is an adjustable (positive) coefficient. The calibration of this coefficient may be exploited  
 216 to account for extraneous effects, such as the possibility that the waves are non-monochromatic,  
 217 and the fact that the current profile is not perfectly logarithmic. Assuming that  $\gamma$  is constant with  
 218 depth is likely to be less accurate outside the surface layer, because the above assumptions about  
 219 the behavior of  $\overline{w'^2}$  and  $dU/dz$  as  $z \rightarrow 0$  do not hold anymore, but the model is not applicable there  
 220 anyway.

221 Note that (8) has the properties of approaching the usual definition of the total shear stress as  
 222 either  $|z| \rightarrow \infty$  or  $La_t \rightarrow \infty$ , both of which make sense physically. The usual wall-layer scaling  
 223 for the dissipation rate, consistent with (3) and with a logarithmic current profile, was shown to  
 224 hold by the observations of various authors at sufficiently large depths (Gargett 1989, Agrawal  
 225 et al. 1992, Terray et al. 1996), and is obviously recovered when the influence of surface waves  
 226 becomes vanishingly small (which corresponds to  $La_t \rightarrow \infty$ ) (McLeish and Putland 1975, Kondo  
 227 1976). The remaining part of the shear stress,  $\overline{u'w'} - (\overline{u'w'})_s$ , is evidently wave-related, and ap-

228 proaches zero when either  $|z| \rightarrow \infty$  or  $La_t \rightarrow \infty$ . Its depth of penetration is clearly, from (8),  
 229 of  $O(1/(2k_w))$ , although it should be borne in mind that this particular dependence results di-  
 230 rectly from the monochromatic wave approximation. Other approaches to treat the dependence  
 231 of  $(dU_S/dz)/(dU/dz)$  (as well as that of  $\overline{u'^2}/\overline{w'^2}$ ) with depth could result in different functional  
 232 forms for  $(\overline{u'w'})_s$ , with  $\gamma$  possibly not being treated as a constant.

233 An interesting property of (8) is that, when evaluated at the surface, it allows the definition of a  
 234 modified friction velocity affected by shear,  $u_{*s}$ , as

$$u_{*s} = -\frac{(\overline{u'w'})_s}{u_*} = \frac{u_*}{1 + \gamma La_t^{-2}}. \quad (9)$$

235 Clearly,  $u_{*s}$  is always smaller than  $u_*$ , and can even become much smaller when  $La_t$  is low. This  
 236 is in agreement with LES results by, e.g., McWilliams et al. (1997), Li et al. (2005) and Grant and  
 237 Belcher (2009) showing that shear in the current profile decreases markedly for a constant wind  
 238 stress  $\tau$  as  $La_t$  decreases (see section 3). One advantage of (9) is that it allows the definition of  
 239 friction velocities due to shear and due to the wave that are additive, yielding the sum  $u_*$ . The  
 240 present approach partially resembles the modification of the surface shear stress to account for  
 241 wave effects in the study of the Ekman-Stokes boundary layer by Polton et al. (2005), where,  
 242 however, the Earth's rotation effect was taken into account.

### 243 *c. A model for the current profile*

244 To obtain a model for the current profile that is consistent with the existing surface layer theory,  
 245 a first-order turbulence closure is applied to the shear-related shear stress, namely

$$(\overline{u'w'})_s = -K_m \frac{dU}{dz}, \quad (10)$$

246 where  $K_m = \kappa u_* |z|$ , as usually defined. Here  $u_*$  is taken as the relevant velocity scale for momen-  
 247 tum transport, since the vertical velocity fluctuations, which effect this transport, scale on  $u_*$  rather

248 than on  $u_{*s}$ . Then the shear of the mean current can be expressed as

$$\frac{dU}{dz} = -\frac{(\overline{u'w'})_s}{\kappa u_* |z|} = \frac{u_*}{\kappa |z|} \phi_L(La_t, k_w |z|), \quad (11)$$

249 where (8) has been used in the second equality, and

$$\phi_L(La_t, k_w |z|) = \frac{1}{1 + \gamma La_t^{-2} e^{-\varepsilon k_w |z|}}, \quad (12)$$

250 where  $\varepsilon = 2$  from (8), but will hereafter be kept as an adjustable parameter for maximum gener-  
 251 ality. As for  $\gamma$ , the adjustment of  $\varepsilon$  may be exploited to account for various extraneous effects,  
 252 such as the presence of non-monochromatic waves. The connection with this latter aspect is even  
 253 closer, since  $\varepsilon$  controls the vertical penetration of wave effects, which may depend not only on the  
 254 dominant wavelength, but also on the wave energy distribution by scale.

255 Note that  $\phi_L$  plays in (11) a role analogous to that played by stability functions in Monin-  
 256 Obukhov theory of the non-neutral surface layer. The difference resides in the fact that  $\phi_L$  depends  
 257 on wave quantities (according to (12)) instead of on stratification. This formulation is amenable to  
 258 improvement, since the form of (12) only needs to be modified to account for missing effects or  
 259 a more accurate representation of the effects already considered. The form taken by (11) implies  
 260 that both at large depths (where usual surface layer scaling is recovered) and near the surface  $z \approx 0$   
 261 the current profile is approximately logarithmic, but with different friction velocities  $u_*$  and  $u_{*s}$ ,  
 262 respectively, as expressed by (9). The dependence of (12) on  $z$  is, arguably, the simplest possible  
 263 that benefits from these properties. The partition of the shear stress into shear-induced and wave-  
 264 induced components, conjugated with the use of a first-order turbulence closure (10), parallels the  
 265 approach, used in a numerical modeling context, of Harcourt (2013). However, the partition itself  
 266 was originally suggested by Teixeira (2011a) based on the shear stress budget (5), and used in the  
 267 present form by Teixeira (2012).



268 From (10), (11) and (12) it is possible to define an ‘effective’ eddy viscosity  $K_m^*$  that takes into  
 269 account wave effects:

$$K_m^* = -\frac{\overline{u'w'}}{dU/dz} = \kappa u_* |z| \left( 1 + \gamma La_t^{-2} e^{-\varepsilon k_w |z|} \right). \quad (13)$$

270 Its form clearly shows the apparent mixing enhancement resulting from the reduction of  $dU/dz$ .

271 To complete the model, it remains to integrate (11) between  $z = z_0$  (where  $U = U_0$ ,  $U_0$  being the  
 272 Eulerian current at the surface), and a generic  $z$ . This yields

$$U_0 - U(z) = \frac{u_*}{\kappa} \int_{z_0}^{|z|} \frac{1}{z'} \frac{1}{1 + \gamma La_t^{-2} e^{-\varepsilon k_w z'}} dz'. \quad (14)$$

273 If velocities are normalized by  $u_*$  and  $|z|$  by  $k_w$ , (14) may be rewritten

$$\frac{U_0 - U(z)}{u_*} = \frac{1}{\kappa} \int_{k_w z_0}^{k_w |z|} \frac{1}{z'} \frac{1}{1 + \gamma La_t^{-2} e^{-\varepsilon z'}} dz'. \quad (15)$$

274 Often, current profiles in the surface layer are specified using so-called wall-coordinates, defined  
 275 as  $U^+ = (U_0 - U(z))/u_*$  and  $z^+ = |z|u_*/\nu$ , where  $\nu$  is the kinematic viscosity of water. Using these  
 276 definitions, (15) can be expressed as

$$U^+ = \frac{1}{\kappa} \int_{\frac{k_w \nu}{u_*} \frac{z_0 u_*}{\nu}}^{\frac{k_w \nu}{u_*} z^+} \frac{1}{z'} \frac{1}{1 + \gamma La_t^{-2} e^{-\varepsilon z'}} dz'. \quad (16)$$

277 The advantage of expressing the lower limit of integration in this form is that for aerodynamically  
 278 smooth flow,  $z_0 u_*/\nu = 0.11$  (Cheung and Street 1988, Kraus and Businger 1994), a result that  
 279 will be used below. The integral in (15) or (16) cannot in general be evaluated analytically. For  
 280 numerical evaluation purposes only, it is useful to introduce the further change of variable  $z' =$   
 281  $\exp \zeta$ , which transforms (16) into

$$U^+ = \frac{1}{\kappa} \int_{\log\left(\frac{k_w \nu}{u_*} \frac{z_0 u_*}{\nu}\right)}^{\log\left(\frac{k_w \nu}{u_*} z^+\right)} \frac{1}{1 + \gamma La_t^{-2} e^{-\varepsilon \exp \zeta}} d\zeta. \quad (17)$$

282 This eliminates the singularity at  $z' = 0$ , which is especially bothersome for small values of  $z_0$ .

283 In the limit  $La_t \rightarrow \infty$ , (17) (or (16)) can, of course, be integrated analytically, reducing to

$$U^+ = \frac{1}{\kappa} \log \left( \frac{z^+ \mathbf{v}}{z_0 u_*} \right) = \frac{1}{\kappa} \log \left( \frac{|z|}{z_0} \right). \quad (18)$$

284 For aerodynamically smooth flow, (18) further reduces to

$$U^+ = \frac{1}{\kappa} \log \left( \frac{z^+}{0.11} \right) = \frac{1}{\kappa} \log z^+ + 5.5, \quad (19)$$

285 as noted by Cheung and Street (1988), where it was assumed that  $\kappa = 0.4$ .

286 When plotted with a logarithmic scale for depth, (17) consists of two straight line segments  
 287 separated by a transition depth interval centered around  $|z| \approx 1/(\epsilon k_w)$ . The slope of the current  
 288 profile in its upper, wave-affected part, is consistent with the reduced friction velocity  $u_{*s}$ , given  
 289 by (9), i.e.,

$$\frac{dU}{dz}(z \rightarrow 0) = \frac{u_{*s}}{\kappa|z|} \quad (20)$$

290 (as results from (9), (11) and (12)), and  $u_*$  is of course consistent with the slope of the profile  
 291 segment occurring at larger depths (see discussion below). The roughness length  $z_0$  is the height  
 292 at which  $U^+ = 0$ , irrespective of whether the current profile is affected by waves or not. In the  
 293 latter case, an apparent roughness length can be defined, which corresponds to the intersect of the  
 294 prolongation of the segment of the current profile at large depths with the axis where  $U^+ = 0$ . It  
 295 can be anticipated that this apparent roughness length  $z_{0w}$  is much larger than the true  $z_0$  when  
 296 the effect of waves is important, because of the break point (or more precisely transition region)  
 297 existing in the current profile.  $z_{0w}$  can be obtained by integrating (11) between  $z_0$  and  $\infty$  and then  
 298 (3) back to  $z_{0w}$ . This yields

$$\log(k_w z_{0w}) = \log(k_w z_0) + \gamma La_t^{-2} \int_{\log(k_w z_0)}^{\infty} \frac{e^{-\epsilon \exp \zeta}}{1 + \gamma La_t^{-2} e^{-\epsilon \exp \zeta}} d\zeta. \quad (21)$$

299 Equations (9), (17) and (21) form the basis of the calculations presented in this paper.

300 It is worth noting that the formulation of the shear stress on which these equations are based,  
 301 (10), is strictly local, neglecting any transport effects, whereby  $dU/dz$  might become negative with  
 302  $\overline{u'w'}$  remaining also negative (corresponding to a negative eddy viscosity in (10)). This behavior,  
 303 which is produced in a number of LES results (McWilliams et al. 1997, Li et al. 2005, Tejada-  
 304 Martinez et al. 2013), was recently parameterized by Sinha et al. (2015) by adopting a non-local  
 305 component of the shear stress, akin to those used in momentum flux parameterizations for convec-  
 306 tion. Since the data used in the present study (from Cheung and Street 1988) do not show such  
 307 negative current shear (another example is the top surface layer in Fig. 5 of Longo et al. (2012)),  
 308 that approach is not used here, although it may be viewed as one of the possible improvements to  
 309 the present scheme.

### 310 1) MODEL FOR A LINEARLY DECREASING SHEAR STRESS

311 For the purpose of comparing the model developed above with the laboratory measurements of  
 312 Cheung and Street (1988) (to be done below), it is convenient to assume that the shear stress is not  
 313 constant with depth, but rather varies linearly from its maximum at the air-water interface to zero  
 314 at a certain depth. This parallels the approach used by Cheung and Street (1988) to estimate the  
 315 shear stress from their data, and corresponds mathematically to

$$\overline{u'w'} = -u_*^2 \left(1 - \frac{|z|}{\delta}\right) \quad \text{if } |z| \leq \delta, \quad (22)$$

316 where  $\delta$  is the depth where  $\overline{u'w'}$  becomes zero, and it is implied that for  $|z| > \delta$ ,  $\overline{u'w'} = 0$ . In this  
 317 case, the function  $\phi_L$  must be redefined (for  $|z| \leq \delta$ ) as

$$\phi_L \left( La_t, k_w |z|, \frac{|z|}{\delta} \right) = \frac{1 - \frac{|z|}{\delta}}{1 + \gamma La_t^{-2} e^{-\epsilon k_w |z|}}, \quad (23)$$

318 and (11) may then be integrated to give

$$U^+ = \frac{1}{\kappa} \int_{\frac{k_w v}{u_*}}^{\frac{k_w v}{u_*} z^+} \left( \frac{1}{z'} - \frac{1}{k_w \delta} \right) \frac{1}{1 + \gamma La_t^{-2} e^{-\epsilon z'}} dz' \quad (24)$$

319 (again valid only for  $|z| \leq \delta$ ), replacing (16). For  $|z| > \delta$ ,  $U^+ = U^+(z^+ = \delta u_* / v)$ , which is a  
 320 constant. In the limit  $La_t \rightarrow \infty$ , (24) reduces to

$$U^+ = \frac{1}{\kappa} \left[ \log(z^+) - \frac{z^+}{\frac{\delta u_*}{v}} - \log\left(\frac{z_0 u_*}{v}\right) + \frac{z_0}{\delta} \right], \quad (25)$$

321 which has a log-linear variation and must replace (19).

322 Note that, according to (10) and (22), for  $|z| > \delta$ ,  $dU/dz = 0$  under the present assumptions,  
 323 i.e., no mean shear exists and the current speed does not vary. This gives the version of the model  
 324 just described the capability of predicting the surface value of the wind-induced current (unlike  
 325 the version described in the previous subsection, where  $U$  varies indefinitely). Defining arbitrarily  
 326  $U(|z| = \delta) = 0$ , which makes sense since this is the value of the current at the depth where the  
 327 effect of the surface wind stress is no longer felt, then from the definition of  $U^+$  it follows that  
 328  $U_0/u_* = U^+(|z| = \delta) = U^+(z^+ = \delta u_* / v)$ , which can be obtained from (24).

329 As a caution, it should be emphasized that the assumption of a non-constant shear stress, ex-  
 330 pressed by (22), may not be strictly consistent with statistically steady and horizontally homoge-  
 331 neous flow (implicit in surface layer theory), requiring either a time evolution of the mean current  
 332 or a mean horizontal pressure gradient, but hopefully this assumption is still acceptable for the  
 333 present purposes. A model with a linearly decreasing shear stress, such as the one just presented,  
 334 might be thought of as a very simple representation of the whole oceanic boundary layer (of depth  
 335  $\delta$ ) instead of just the surface layer. However, its applicability to real cases is limited by neglect  
 336 of the effect of the Earth's rotation, the choices made to approximate (7) as (8), and the Monin-  
 337 Obukhov approach inherent to (11) and (12). These are confined to the surface layer, and would  
 338 require modification in order to extend the model.

### 339 3. Results

340 It is instructive first of all to explore the model behavior for a few representative cases, because  
341 this illustrates in the ‘cleanest’ possible way the range of behavior of the model and its impact on  
342 the perceived values of the water-side values of  $u_*$  and  $z_0$ . More detailed comparisons with labo-  
343 ratory experiments follow. In all of these cases,  $\gamma$  and  $\varepsilon$  will be treated as adjustable parameters.

#### 344 a. Generic behavior of the model

345 Figure 1 shows profiles of  $U^+$  as a function of  $k_w|z|$  from (15) for  $k_w z_0 = 0.001$  and different  
346 values of the turbulent Langmuir number  $La_t = 0.5, 1, 2$ , assuming that  $\gamma = 1$  and  $\varepsilon = 1$ , for  
347 simplicity. Note that these values of  $\gamma$  and  $\varepsilon$  are of the same order of magnitude as those adopted  
348 by Teixeira (2012). The results are not qualitatively very sensitive to  $k_w z_0$  in the representation  
349 adopted in Fig. 1, and variation of this parameter merely leads to a rescaling of the horizontal axis,  
350 with a narrower transition region between the two logarithmic portions of the curves occurring for  
351 values of  $k_w z_0 \ll 1$ .

352  $La_t = 2$  intends to represent shear-dominated turbulence,  $La_t = 0.5$  Langmuir (i.e., wave-  
353 dominated) turbulence, and  $La_t = 1$  turbulence with a transitional character. As can be seen in  
354 Fig. 1, the current profiles (denoted by the solid curves) have a lower portion with invariant slope  
355 for larger depths. This slope, when expressed in terms of  $U^+/\log|z|$ , is  $1/\kappa$ , because of the way  
356  $U^+$  is normalized. At smaller depths the current profile has a lower slope (prolonged to larger  $|z|$  as  
357 the dashed asymptotes), which is proportional to the values of the ratio  $u_{*s}/u_*$  in each case. From  
358 (9) (for  $\gamma = 1$ ), these values are  $u_{*s}/u_* = 0.8$  for  $La_t = 2$ ,  $u_{*s}/u_* = 0.5$  for  $La_t = 1$  and  $u_{*s}/u_* = 0.2$   
359 for  $La_t = 0.5$ . On the the other hand, if the lower portion of the current profile is prolonged towards  
360 the surface (dotted line asymptotes), one obtains an “effective” value of the roughness length, ex-  
361 pressed by (21), which would be obtained by ignoring the upper portion of the current profile. For

362  $La_t = 2$ ,  $k_w z_{0w} = 0.004$ , for  $La_t = 1$ ,  $k_w z_{0w} = 0.030$  and for  $La_t = 0.5$ ,  $k_w z_{0w} = 0.341$ , which shows  
363 dramatically how  $z_{0w}$  may become various orders of magnitude larger than  $z_0$  as  $La_t$  decreases (see  
364 further discussion below).

365 Note that, according to the present model, if measurements are taken at a range of depths well  
366 below the transition region located around  $|z| \approx 1/(\epsilon k_w)$ , the friction velocity corresponding to  
367 the total momentum flux  $u_*$  will be diagnosed correctly from the current profile, but the roughness  
368 length  $z_0$  will be strongly overestimated as  $z_{0w}$ . Conversely, if measurements are taken at a range  
369 of depths above this transition region (if that is feasible),  $z_0$  will be correctly diagnosed from the  
370 current profile, but  $u_*$  will be underestimated as  $u_{*s}$ . Data taken from an intermediate depth range  
371 coinciding with the transition between the two asymptotic portions of the profile (if they form a  
372 reasonably straight line in a logarithmic scale) will lead both to an overestimation of  $z_0$  and to an  
373 underestimation of  $u_*$ . It is likely that at least one of these three possibilities occurs in a large  
374 fraction of the available field or laboratory measurements of wave-affected mean currents.

375 Circumstantial evidence that this is so is provided by the reported need to change (more specifi-  
376 cally decrease) the value of the von Kármán constant to achieve an adequate collapse of measured  
377 current profiles in wall coordinates (Howe et al. 1982, Cheung and Street 1988, Craig and Banner  
378 1994, Siddiqui and Loewen 2007), unless the friction velocity used to define  $U^+$  is that diagnosed  
379 from the current profile itself, here defined as  $u_{*s}$  (Siddiqui and Loewen 2007), which masks this  
380 problem. Clearly, neither of these procedures is very satisfactory, given their arbitrariness. More  
381 evidence supporting the discussion in the preceding paragraph is provided by the consistently high  
382 reported values of the roughness length diagnosed from current profiles, exceeding by orders of  
383 magnitude the value that would be expected from the morphology of the air-water interface, or  
384 the flow regime (Csanady 1984, Burchard 2001, Soloviev and Lukas 2003, Sullivan et al. 2004,  
385 Kudryavtsev et al. 2008)). Yet more indications, of a more doubtful but suggestive nature, are

386 provided by the fact that the slope of wave-affected currents plotted in wall-layer coordinates in-  
387 creases in some cases at larger depths (see, e.g., the diamond and circle symbols in Fig. 1 of  
388 Cheung and Street (1988), or the black circles and diamonds in Fig. 6 of Siddiqui and Loewen  
389 (2007)).

390 Although both a decrease of the friction velocity and an increase of the roughness length, as  
391 diagnosed from current profiles, might be expected as a result of vertical mixing of momentum  
392 due to wave breaking, the remarkable property of the model proposed here is that this phenomenon  
393 arises simply due to the partition of the shear stress imposed by non-breaking waves, something  
394 that can be traced back to the production terms of the shear stress budget (5), and is thus much  
395 easier to pinpoint physically. It is, of course, possible, and even likely, that both processes act  
396 in concert when wave breaking does occur, but it is striking that the present mechanism does not  
397 require wave breaking.

398 Figure 2 shows the variation of  $u_{*s}/u_*$  as a function of  $La_t$  for different values of the calibrating  
399 constant  $\gamma$ , from (9). Unsurprisingly, this ratio takes values that range from  $\approx 1$  for large  $La_t$  to  
400  $\ll 1$  for small  $La_t$ . Clearly, what matters for a correct representation of the variation in between is  
401 the value of  $\gamma$ , with large values corresponding to strong wave effects and small values to weaker  
402 wave effects. This partition of the friction velocity, or between the corresponding shear-induced  
403 and wave-induced stresses, is not an often measured or calculated quantity, but Fig. 5 of Bourassa  
404 (2000) presents an example with some relevance, even if a quantitative comparison is not easy. If  
405 an increase in wind speed is equated with a decrease of  $La_t$  (an idea that is suggested by the com-  
406 parisons of the next subsection), and the ratio of the aqueous shear stress to the total atmospheric  
407 stress is equated with  $u_{*s}/u_*$  (which must at least be partially correct because the aqueous stress  
408 is estimated from current profiles), the decreasing trend of this ratio with increasing wind speed in  
409 Fig. 5 of Bourassa (2000) is consistent with Fig. 2. Another aspect that suggests this reasoning

410 is sound is the leveling off of the stress ratio for the highest wind speeds in Fig. 5 of Bourassa  
 411 (2000). This is clearly consistent with a smaller sensitivity of  $La_t$  to the wind speed at the highest  
 412 wind speeds, which is corroborated by the comparisons presented in the next subsection. Both  
 413 results are compatible with the established idea that in well-developed seas in the real ocean,  $La_t$   
 414 becomes largely independent of the wind speed.

415 Figure 3 presents the variation of  $k_w z_{0w}$  and  $z_{0w}/z_0$  as a function of  $La_t$  from (21) for  $\gamma = 1$   
 416 and  $\varepsilon = 1$  (as assumed in Fig. 1) and different values of  $k_w z_0$ . As expected,  $k_w z_{0w}$  approaches  
 417  $k_w z_0$  for large values of  $La_t$ , but tends to a value independent of  $k_w z_0$  at small  $La_t$ . What this  
 418 means is that at low  $La_t$ ,  $z_{0w}$  scales with  $k_w^{-1}$  rather than with  $z_0$ , i.e.,  $z_{0w}$  is proportional to the  
 419 wavelength of the dominant waves, not to any property of small-scale capillary waves (neglected  
 420 in the model), or to the amplitude of the dominant waves  $a_w$ . This behavior is confirmed by the  
 421 ratio  $z_{0w}/z_0$ , which only approaches 1 for large values of  $La_t$ , whereas it tends to be very high for  
 422 small  $La_t$ . As is consistent with the behavior of  $k_w z_{0w}$ ,  $z_{0w}/z_0$  at low  $La_t$  is inversely proportional  
 423 to  $k_w z_0$ . Since in real situations  $k_w z_0$  may easily be as small as  $10^{-5}$ , the amplification of the  
 424 apparent roughness length can be very pronounced. A qualitative comparison with Fig. 3 of  
 425 Bourassa (2000) is pertinent. Although the dependence of  $z_0$  (which should probably be taken  
 426 as  $z_{0w}$  in the present notation) with  $u_*$  in that figure cannot be tested quantitatively because wave  
 427 information is missing, and the dependence on  $u_*$  affects both the true value of  $z_0$  (see (26) below)  
 428 and (21) via the definition of  $La_t$ , the important point to retain from Fig. 3 of Bourassa (2000) is  
 429 the enormous amplification of  $z_0$ . Bourassa (2000) notes that  $z_0$  is about  $10^5$  larger than expected  
 430 from Charnock's relation (and therefore much higher than the values estimated for the true  $z_0$  in  
 431 the next subsection).



432 *b. Comparison with Cheung et al. (1988)*

433 Finding adequate datasets to test the present model is challenging, because usually the quantities  
434 required as input to the model are not measured. First of all, measuring current profiles in the field  
435 with the required accuracy is extremely difficult, hence the most relevant studies typically involve  
436 laboratory experiments. Even in those cases, almost invariably not all relevant wave quantities  
437 are measured (Bourassa 2000, Siddiqui and Loewen 2007, Longo et al. 2012), and often the shear  
438 stress is not measured directly, but rather estimated from the current profiles (Bourassa 2000,  
439 Siddiqui and Loewen 2007), which makes comparisons more difficult (the erratic behavior of the  
440 current speeds measured by Siddiqui and Loewen (2007) as a function of the wind speed is another  
441 reason to exclude their data). A notable exception are the laboratory experiments of Cheung and  
442 Street (1988) of the current beneath surface waves generated by the wind. The relevant quantities  
443 are presented in their Table 1. As Kudryavtsev et al. (2008) do for the comparison presented in  
444 their Fig. 10, only wind-generated waves are considered here and the case among these waves  
445 with the lowest wind-speed (where the wave amplitude is so small as to be barely measurable) is  
446 ignored.

447 The experiments with mechanical waves are excluded from this comparison because the assump-  
448 tion of the model that  $dU/dz$  and  $dU_S/dz$  have the same sign may not be strictly satisfied. The  
449 possibility that  $dU/dz$  and  $dU_S/dz$  have opposite signs has been demonstrated by Pearson (2018),  
450 for situations with weak (or no) wind, when turbulence exists beneath a wave field. This leads to  
451 a suppression of the instability to Langmuir circulations (which requires  $(dU/dz)(dU_S/dz) > 0$ ),  
452 modifying the stress partition assumed in (8), which relies on the existence of that instability  
453 (Teixeira 2011a).

454 For a reasonable range of input parameters, the present model predicted almost no difference  
 455 between the current profiles beneath wind waves for the two lowest wind speeds in Table 1 of  
 456 Cheung and Street (1988). This justifies (following Kudryavtsev et al. (2008)) ignoring the profile  
 457 for the lowest wind speed,  $1.5 \text{ m s}^{-1}$ , which has a roughness length smaller than that expected for  
 458 an aerodynamically smooth flow, and might be affected by some inaccuracy.

#### 459 1) UNBOUNDED MODEL

460 The first comparison to be made uses an uncalibrated version of the ‘unbounded’ model de-  
 461 scribed in section 2c. The values of  $u_*$  from Table 1 of Cheung and Street (1988) are used directly  
 462 in the model, the wave orbital velocity  $a_w k_w c_w$  is taken as  $\sqrt{2}(\bar{u}_0^2)^{1/2}$ , where  $(\bar{u}_0^2)^{1/2}$  is the root-  
 463 mean-square orbital velocity in the data (as is consistent with Eqs. (4)-(5) of Cheung and Street  
 464 (1988), where  $\hat{\eta}_S$  is equivalent to  $a_w$  here), the angular frequency  $\sigma_w$  is equated to  $2\pi f_D$ , where  
 465  $f_D$  is the frequency (in cycles) of the dominant waves, and the corresponding wavenumber is  
 466  $k_w = \sigma_w^2/g$  from the linear dispersion relation of deep-water surface gravity waves. Some key  
 467 parameters are presented in Table 1. An evidently crucial detail is how to define  $z_0$ . As a first  
 468 approximation the definition valid for aerodynamically smooth flow is adopted:  $z_0 = 0.11\nu/u_*$   
 469 (Kraus and Businger 1994), with  $\nu = 10^{-6} \text{ m}^2 \text{ s}^{-1}$ . Figure 4 shows a comparison of the model  
 470 with the data presented in Fig. 1 of Cheung and Street (1988) (excluding the upward pointing  
 471 triangles for the reasons explained above), assuming  $\varepsilon = 2$  and  $\gamma = 2$ , as in Teixeira (2012) (Fig.  
 472 4a) and using  $\varepsilon = 0.5$  and  $\gamma = 0.5$  (adjusted values) (Fig. 4b).

473 It can be seen in Fig. 4a that the behavior of the measured currents is reasonably well reproduced  
 474 qualitatively, with a decrease of the overall normalized current speed as the wind speed increases.  
 475 In terms of the input parameters of the model, this is due to a decrease of the turbulent Langmuir  
 476 number  $La_t$  as the wind speed increases for the lowest wind speeds, but mostly due to an increase

477 in penetration of the wave motion at the highest wind speeds, for which  $La_t$  actually changes very  
478 little (see Table 1). Noteworthy disagreements are that the range of variation of the current speed  
479 in the model is much too wide compared with the data, in particular, the current speed in wall  
480 coordinates is overestimated for the lowest wind speed and quite underestimated for the highest  
481 wind speeds. Additionally, although two logarithmic portions of the current profile exist in the  
482 model at the highest wind speeds (lowest values of  $La_t$ ), these portions do not coincide with the  
483 data that show a reduced slope (e.g., stars and open circles). Finally, the detailed variation with  
484 the wind speed is not reproduced. While most of the variation occurs at the lowest wind speeds  
485 in the model and weakens roughly monotonically as  $La_t$  decreases, the rate of variation seems to  
486 increase again at the highest wind speeds in the data.

487 When Fig. 4a is compared with Fig. 10 of Kudryavtsev et al. (2008), it may be noticed that the  
488 agreement with the data is somewhat less satisfactory. Although the performance of the model of  
489 Kudryavtsev et al. (2008) is itself far from perfect, its consideration of the effect of the viscous  
490 boundary layer for the current profile with the lowest wind speed substantially improves the agree-  
491 ment at small depths compared with the present model. Additionally, the model of Kudryavtsev  
492 et al. (2008) does not underestimate the current as much at the highest wind speeds. Curiously, it  
493 has some deficiencies similar to those of the present model, namely it overestimates the sensitiv-  
494 ity of the normalized current to the wind speed at intermediate values of that parameter and, on  
495 the contrary, has a too weak dependence for the highest values. On the other hand, the model of  
496 Kudryavtsev et al. (2008) is unable to capture the apparent reduction of  $u_*$  by the wave stress, but  
497 a somewhat similar effect is mimicked by the transition of the profiles to their viscous boundary  
498 layer form (also partly affected by wave breaking).

499 Clearly, the comparison presented in Fig. 4a indicates an overestimation of parameter  $\gamma$  in the  
500 present model. One might wonder why this happens, given that this calibration seemed to work

501 for predictions of the dissipation rate by Teixeira (2012), and also in his preliminary calibration  
 502 procedure using current profiles from the LES of Li et al. (2005). Possible reasons are speculative,  
 503 but might have to do with inadvertently accounting for the effect of wave breaking in the first case,  
 504 and adopting a value of  $\gamma$  suitable for monochromatic waves in the second, both conditions which  
 505 are not applicable here. It seems fortuitous that both of these distinct differences should lead to a  
 506 similar value of  $\gamma$ .

507 In order to improve agreement with the data of Cheung and Street (1988),  $\gamma$  and  $\varepsilon$  may be  
 508 readjusted. Figure 4b shows a comparison similar to that of Fig. 4a, but where  $\gamma = 0.5$  and  $\varepsilon = 0.5$   
 509 are assumed, presumably to account for both the absence of wave breaking in the experiments of  
 510 Cheung and Street (1988) and the fact that the waves are non-monochromatic. The adjusted values  
 511 of these parameters improve the agreement, particularly for the dataset with the highest wind speed  
 512 (making it almost perfect by construction), but this turns out not to be sufficient. The variation of  
 513 the normalized current speed for intermediate wind speeds is still affected by the problems pointed  
 514 out above.

515 It is likely that the flow in the experiments under consideration was not always aerodynami-  
 516 cally smooth, but rather becomes aerodynamically rough at the highest wind speeds, because of  
 517 the small-scale corrugations forced at the air-water interface by the wind stress. A form of the  
 518 roughness length that reflects this is

$$z_0 = c_1 \frac{\nu}{u_*} + c_2 \frac{u_*^2}{g}, \quad (26)$$

519 where  $c_1$  and  $c_2$  are coefficients, and the second term is of a form analogous to the Charnock  
 520 relation, but using the friction velocity in the water. In what follows,  $\gamma$ ,  $\varepsilon$ ,  $c_1$  and  $c_2$  are adjusted to  
 521 produce the best possible agreement with the data of Cheung and Street (1988). The values found  
 522 for the unbounded model are  $\gamma = 0.25$ ,  $\varepsilon = 0.5$ ,  $c_1 = 0.2$  and  $c_2 = 0.9$ .

523 Figure 5a shows a comparison of the model with the data of Cheung and Street (1988) using  
524 these adjusted parameters. The agreement is much better than in Fig. 4, in particular for the rate  
525 of variation of the normalized current profiles at intermediate wind speeds (this is not surprising,  
526 being a result of the calibration procedure). Agreement is less close for the lowest wind speed  
527 considered at small depths, due to the absence of a viscous boundary layer in the model, but this is  
528 a minor limitation. The transition of the datasets from a slope corresponding to  $u_*$  to the smaller  
529 value corresponding to  $u_{*s}$  is fairly well reproduced, occurring somewhere around between the  
530 wind speeds of 4.7 and 6.7  $\text{ms}^{-1}$ . However, at these intermediate wind speeds, the current at the  
531 smallest depths covered by the data is somewhat underestimated by the model (the shear suggested  
532 by the data at those depths is weaker than expected). Additionally while the current is slightly  
533 underestimated for a wind speed of 4.7  $\text{ms}^{-1}$ , it is on the contrary slightly overestimated for a  
534 wind speed of 3.2  $\text{ms}^{-1}$ . It is perhaps risky to attach too much relevance to these discrepancies in  
535 detail, given the limited precision of the measurements (which are, nevertheless, among the most  
536 precise that could be found).

537 The value of  $\gamma$  was already discussed above. The value of  $\varepsilon$  adopted for this comparison would  
538 correspond to the Stokes drift of a monochromatic wave with a wavelength 4 times larger than the  
539 wavelength of the dominant waves, obtained from the data. The significance of this mismatch for  
540 non-monochromatic waves (such as the ones under consideration) is not obvious, but indicates a  
541 larger depth of penetration of the wave-induced stress than would be expected. The Stokes drift  
542 gradient of a wave spectrum is known to be characterized by a larger penetration depth than a  
543 monochromatic wave with the same dominant wavelength (Fig. 18 of Li and Garrett (1993)), and  
544 this may perhaps account for a similar effect on the wave-induced stress.

545 Concerning parameters estimated for (26),  $c_1 = 0.2$  is substantially larger than the value of  
546 0.11 most commonly accepted for aerodynamically smooth flow. It is worth noting that, in Fig.

547 10 of Kudryavtsev et al. (2008) the thin line (corresponding to aerodynamically smooth flow)  
548 assumes  $z_0 = 0.18\nu/u_*$ , which is not too different from the value employed here. Regarding  $c_2$ ,  
549 the Charnock relation, when expressed in terms of the friction velocity in the airflow, usually has  
550 a coefficient of 0.015. Taking into account continuity of the shear stress at the air-water interface,  
551 when that relation is expressed in terms of the friction velocity in the water the coefficient should  
552 become  $833 \times 0.015 = 12.5$ . This is clearly much larger than  $c_2 = 0.9$  used here, but it should be  
553 noted that the Charnock relation, as usually formulated, is valid in the open ocean and for a fully-  
554 developed wave field, which are very distinct conditions from those produced in the experiments  
555 of Cheung and Street (1988). Additionally, continuity of the shear stress at the air-water interface  
556 (used in the above calculation) assumes equilibrium, which is not warranted in these experiments  
557 either. Nevertheless, a reassuring aspect is that, on dimensional grounds, the quantities on which  
558 (26) depends are still likely to be the most relevant.

559 It might be argued that the agreement between model and measurements in Fig. 5a was arti-  
560 ficially improved by allowing  $z_0$  to vary according to (26). To test this, Fig. 5b shows a similar  
561 comparison, but where wave effects are ignored altogether, and only the dependence of  $z_0$  on  $u_*$   
562 via (26) is retained (with similar values of  $c_1$  and  $c_2$ ). It is clear that this dependence, by itself, is  
563 unable to produce a satisfactory agreement with the measurements, particularly at the highest wind  
564 speeds, and naturally does not represent the decrease of the apparent value of  $u_*$ , although it does  
565 represent a part of the increase of  $z_0$  required to match the data. Relatedly, (26) contributes signif-  
566 icantly to the weakening of the the current speed at the highest wind speeds, which is important to  
567 improve agreement with the data relative to Fig. 4.

568 2) FINITE-DEPTH MODEL

569 Figure 6 shows a similar comparison to Fig. 5, but using the finite-depth model developed in  
570 section 2c1. Because of the log-linear form of the current profile, the current solutions are no  
571 longer composed of straight line segments when using a logarithmic depth scale, but tend to have  
572 a reduction in shear at the depths near where the shear stress becomes zero (and the current speed  
573 stabilizes), marked by the vertical lines in Fig. 6. Below those levels the shear obviously becomes  
574 zero, as is denoted by the horizontal lines in Fig. 6. However, some modified form of the current  
575 slope transition at depth  $|z| \approx 1/(\varepsilon k_w)$  still holds, as can be inferred from Fig. 6, if that depth is  
576 above the level where the shear stress vanishes (which always happens in the data of Cheung and  
577 Street (1988) – see Table 1). The parameter values used in Fig. 6 are  $\gamma = 0.25$ ,  $\varepsilon = 1$ ,  $c_1 = 0.2$  and  
578  $c_2 = 0.9$ . The agreement between the model and measurements is roughly as satisfactory as in Fig.  
579 5, with essentially the same deficiencies in the mid-range of wind speeds. At the largest depths  
580 considered (near to  $|z| = \delta$ ) the model tends to underestimate the measurements more, perhaps  
581 because the reduction of shear in those regions is too large due to the assumption of a linearly  
582 decreasing shear stress. In reality, the fact that the shear stress decays to zero more gradually  
583 might explain why no marked reduction in the shear is detectable in the data at those depths. The  
584 existence of this shear reduction in the model counteracts the transition to a larger shear that occurs  
585 below the depth  $|z| \approx 1/(\varepsilon k_w)$ , when this is not too distant from  $|z| = \delta$ . This is what allows a  
586 larger value of  $\varepsilon$  to be employed in Fig. 6.

587 A noteworthy property of this finite-depth model is that it enables an estimation of the magnitude  
588 of the surface current speed  $U_0$ , as noted in section 2c1. Figure 7 shows a comparison of the values  
589 of  $U_0/u_*$  calculated from the model (corresponding to the horizontal portions of the curves in Fig.  
590 6) with the values that can be either obtained directly from Table 1 of Cheung and Street (1988)

591 (circles), or obtained from the data point with the largest depth in the datasets for each wind speed  
592 in Fig. 6 (triangles). It can be seen that the agreement is encouraging, with correlation coefficients  
593 of  $\approx 0.95$  in both cases, although the model does tend to systematically underestimate the data.  
594 However, given the strong assumptions adopted, the agreement is surprisingly good.

#### 595 **4. Concluding remarks**

596 This study presents a simple model for the wind-driven current existing in the oceanic boundary  
597 layer in the presence of surface waves generated by the wind. The model sheds light on two  
598 puzzling aspects that have been noted repeatedly about these currents, for which a logarithmic  
599 profile model, with the friction velocity  $u_*$  and roughness length  $z_0$  as basic parameters, has often  
600 been adopted. Firstly, if the current speed is scaled using the total friction velocity, measured  
601 independently, e.g., using the surface wind stress, the friction velocity diagnosed from shear in  
602 the current profile is smaller than expected, being only a fraction of the total friction velocity.  
603 Secondly, the roughness length diagnosed from the same fitting procedure is much larger than  
604 expected, by various orders of magnitude, being inconsistent with the roughness length that would  
605 be estimated either for an aerodynamically smooth flow, or aerodynamically rough flow affected  
606 by waves. The corresponding Charnock parameter appears to be enormously amplified (Bourassa  
607 2000).

608 Both of these features are explained here as resulting from a partition of the total turbulent shear  
609 stress into a shear-induced component and a wave-induced component, which result from the local  
610 mechanical production of this stress by the mean shear in the current profile, and by the Lagrangian  
611 strain rate associated Stokes drift of the waves, respectively, when the effect of non-breaking waves  
612 is included in the equations of motion via the Craik-Leibovich vortex force. In this framework, the  
613 wave-associated part of the shear stress is not a property of the wave itself, as assumed by some



614 authors, but is a stress created, on the turbulence that co-exists with the shear-induced stress, by  
615 Stokes drift straining of turbulent vorticity into the streamwise direction (the assumed direction  
616 of both the mean current and the Stokes drift) (Teixeira 2011a). This is independent from any  
617 vertical mixing associated with pre-existing turbulence, or turbulence injected into the water by  
618 wave breaking.

619 It is likely that this mechanism associated with non-breaking waves acts in concert with other  
620 mechanisms related to wave breaking, and with the transport of turbulence by itself in general, but  
621 the fact that it can account for the two phenomena mentioned above, and that its dependence on  
622 the turbulent Langmuir number appears to be confirmed by measurements, support its relevance.

623 The model predicts that the part of the turbulent shear stress induced by shear in the surface  
624 layer becomes a progressively smaller fraction of the total stress near the surface and down to a  
625 depth of the order the wavelength of the dominant surface waves as  $La_t$  decreases. This leads to  
626 the perceived reduction of the friction velocity. The model also predicts that the roughness length  
627 inferred if the uppermost portion of the current profile is disregarded is amplified by various orders  
628 of magnitude as  $La_t$  decreases, and scales with  $k_w^{-1}$ , i.e., the wavelength of the waves, at small  $La_t$ .  
629 The profile of the wind-induced current becomes flatter (that is, less different from its surface  
630 value) as  $La_t$  decreases.

631 If the parameters in the model are adjusted appropriately, departing from their values assumed  
632 in Teixeira (2012) (presumably to account for the facts that there is no substantial wave break-  
633 ing in the experiments and the waves are not monochromatic), good agreement is found with the  
634 laboratory measurements of Cheung and Street (1988), which appear to be the only dataset that  
635 is precise and comprehensive enough for this purpose. Other more recent datasets (Siddiqui and  
636 Loewen 2007, Longo et al. 2012) either seem unreliable, or do not provide complete enough infor-  
637 mation about the characteristics of the wave field or of the total shear stress. In the experiments of

638 Cheung and Street (1988), the current profile becomes flatter as the wind speed increases. Using  
639 the present model, this is interpreted as being primarily due to a decrease in  $La_t$  at the lowest wind  
640 speeds, and due to an increasingly deeper penetration of the wave stress, conjugated with a higher  
641 real roughness length, at the highest wind speeds.

642 As in the present model, a recent study of Sinha et al. (2015) uses insights from Teixeira (2012)  
643 to develop a turbulence closure that includes wave effects. However, the dataset they use to test  
644 their model, from LES of Tejada-Martinez et al. (2013), refers to shallow water flow, and is thus  
645 strongly affected by the bottom boundary layer. Sinha et al. (2015) primarily focus on an analysis  
646 of the current profile in wall-coordinates within the bottom boundary layer, but the full-depth  
647 current profiles shown by them (e.g., their Figs. 19 and 21) suggest a relatively modest agreement  
648 between their model in the top boundary layer adjacent to the air-water interface, despite the fact  
649 that they include a term in the shear stress definition that is non-local, accounting for turbulent  
650 transport of TKE (which is not considered here).

651 In order to bring the model presented here closer to real oceanic conditions, and thus increase its  
652 usefulness, it is probably not only necessary to account for non-local mixing (which is important  
653 in some datasets), but also for the effect of the Earth's rotation, as wind-driven currents are known  
654 to be typically misaligned with the surface stress and rotate with depth, in accordance with Ekman  
655 layer theory. However, within the surface layer where the shear stress is the primary mechanism  
656 shaping the current, shear at least is necessarily aligned with the wind stress, and thus the model  
657 presented here may still be directly applicable to the streamwise component of the current.

658 Defining precisely the range of applicability of the present model is complicated (when com-  
659 pared to the atmosphere) by the presence of surface waves, as their influence may in some cases  
660 be confined to the oceanic surface layer (as happens here), and in others extend below it. To a first

661 approximation, the surface layer might be defined as the layer in which there is little fractional  
662 change in the vertical of both the shear stress and the current direction.

663 The results reported here are presented in dimensionless form, which should facilitate their trans-  
664 position to real oceanic conditions, enabling the development of physically-based parametrizations  
665 for the turbulent momentum flux in the wave-affected boundary layer for ocean circulation models.

## 666 **References**

667 Agrawal, Y. C., E. A. Terray, M. A. Donelan, P. A. Hwang, A. J. W. III, W. M. Drennan, K. K.  
668 Kahma, and S. A. Kitaigorodskii, 1992: Enhanced dissipation of kinetic energy beneath surface  
669 waves. *Nature*, **359**, 219–220.

670 Bourassa, M. A., 2000: Shear stress model for the aqueous boundary layer near the air-water  
671 interface. *J. Geophys. Res.*, **105**, 1167–1176.

672 Burchard, H., 2001: Simulating the wave-enhanced layer under breaking surface waves with two-  
673 equation turbulence models. *J. Phys. Oceanogr.*, **31**, 3133–3145.

674 Cheung, T. K., and R. L. Street, 1988: The turbulent layer in the water at an air-water interface. *J.*  
675 *Fluid Mech.*, **194**, 133–151.

676 Craig, P. D., 1996: Velocity profiles and surface roughness under breaking waves. *J. Geophys.*  
677 *Res.*, **101**, 1265–1277.

678 Craig, P. D., and M. L. Banner, 1994: Modeling wave-enhanced turbulence in the ocean surface  
679 layer. *J. Phys. Oceanogr.*, **24**, 2546–2559.

680 Csanady, G. T., 1984: The free surface turbulent shear layer. *J. Phys. Oceanogr.*, **14**, 402–411.

- 681 Csanady, G. T., 2004: *Air-Sea Interaction - Laws and Mechanisms*. Cambridge University Press,  
682 239 pp.
- 683 Drennan, W. M., M. A. Donelan, E. A. Terray, and K. B. Katsaros, 1996: Oceanic turbulence  
684 dissipation measurements in swade. *J. Phys. Oceanogr.*, **26**, 808–815.
- 685 Feddersen, F., J. H. Trowbridge, and A. J. W. III, 2007: Vertical structure of dissipation in the  
686 nearshore. *J. Phys. Oceanogr.*, **37**, 1764–1777.
- 687 Gargett, A. E., 1989: Ocean turbulence. *Ann. Rev. Fluid Mech.*, **21**, 419–451.
- 688 Gemmrich, J. R., and D. M. Farmer, 1999: Near-surface turbulence and thermal structure in a  
689 wind-driven sea. *J. Phys. Oceanogr.*, **29**, 480–499.
- 690 Gerbi, G. P., J. H. Trowbridge, E. A. Terray, A. J. Pluddeman, and T. Kukulka, 2009: Observations  
691 of turbulence in the ocean surface boundary layer: energetics and transport. *J. Phys. Oceanogr.*,  
692 **39**, 1077–1096.
- 693 Grant, A. L. M., and S. E. Belcher, 2009: Characteristics of langmuir turbulence in the ocean  
694 mixed layer. *J. Phys. Oceanogr.*, **39**, 1871–1887.
- 695 Harcourt, R. R., 2013: A second-moment closure model of langmuir turbulence. *J. Phys.*  
696 *Oceanogr.*, **43**, 673–697.
- 697 Howe, B. M., A. J. Chambers, S. P. Klotz, T. K. Cheung, and R. L. Street, 1982: Comparison of  
698 profiles and fluxes of heat and momentum above and below an air-water interface. *Trans. ASME*  
699 *C: J. Heat Transfer*, **104**, 34–39.
- 700 Jones, N. L., and S. G. Monismith, 2008: The influence of whitecapping waves on the vertical  
701 structure of turbulence in a shallow estuarine embayment. *J. Phys. Oceanogr.*, **38**, 1563–1580.

- 702 Kondo, J., 1976: Parameterization of turbulent transport in the top meter of the ocean. *J. Phys.*  
703 *Oceanogr.*, **6**, 712–720.
- 704 Kraus, E. B., and J. A. Businger, 1994: *Atmosphere-Ocean Interaction, Second Edition*. Oxford  
705 University Press, 362 pp.
- 706 Kudryavtsev, V., V. Shrira, V. Dulov, and V. Malinovsky, 2008: On the vertical structure of wind-  
707 driven sea currents. *J. Phys. Oceanogr.*, **38**, 2121–2144.
- 708 Kukulka, T., and R. R. Harcourt, 2017: Influence of stokes drift decay scale on langmuir turbu-  
709 lence. *J. Phys. Oceanogr.*, **47**, 1637–1656.
- 710 Kukulka, T., A. J. Plueddemann, J. H. Trowbridge, and P. P. Sullivan, 2010: Rapid mixed  
711 layer deepening by the combination of langmuir and shear instabilities: a case study. *J. Phys.*  
712 *Oceanogr.*, **40**, 2381–2400.
- 713 Lee, M. J., J. Kim, and P. Moin, 1990: Structure of turbulence at high shear rate. *J. Fluid Mech.*,  
714 **216**, 561–583.
- 715 Li, M., and C. Garrett, 1993: Cell merging and the jet/downwelling ratio in langmuir circulation.  
716 *J. Marine Res.*, **51**, 737–769.
- 717 Li, M., C. Garrett, and E. Skillingstad, 2005: A regime diagram for classifying turbulent large  
718 eddies in the upper ocean. *Deep-Sea Res.*, **52**, 259–278.
- 719 Longo, S., D. Liang, L. Chiapponi, and L. A. Jiménez, 2012: Turbulent flow structure in experi-  
720 mental laboratory wind-generated gravity waves. *Coastal. Eng.*, **64**, 1–15.
- 721 McLeish, W. L., and G. E. Putland, 1975: Measurements of wind-driven flow profiles in the top  
722 millimeter of water. *J. Phys. Oceanogr.*, **5**, 516–518.

- 723 McWilliams, J. C., P. P. Sullivan, and C.-H. Moeng, 1997: Langmuir turbulence in the ocean. *J.*  
724 *Fluid Mech.*, **334**, 1–30.
- 725 Pearson, B., 2018: Turbulence-induced anti-stokes flow and the resulting limitations of large-eddy  
726 simulation. *J. Phys. Oceanogr.*, **48**, 117–122.
- 727 Phillips, O. M., 1977: *The Dynamics of the Upper Ocean*. Cambridge University Press, 336 pp.
- 728 Polton, J. A., and S. E. Belcher, 2007: Langmuir turbulence and deeply penetrating jets in an  
729 unstratified mixed layer. *J. Geophys. Res.*, **112**, C09 020.
- 730 Polton, J. A., D. M. Lewis, and S. E. Belcher, 2005: The role of wave-induced coriolis-stokes  
731 forcing on the wind-driven mixed layer. *J. Phys. Oceanogr.*, **35**, 444–457.
- 732 Rasche, N., and F. Ardhuin, 2009: Drift and mixing under the ocean surface revisited: stratified  
733 conditions and model-data comparisons. *J. Geophys. Res.*, **114**, C02 016.
- 734 Rasche, N., F. Ardhuin, and E. A. Terray, 2006: Drift and mixing under the ocean surface: a  
735 coherent one-dimensional description with application to unstratified conditions. *J. Geophys.*  
736 *Res.*, **111**, C03 016.
- 737 Siddiqui, M. H. K., and M. R. Loewen, 2007: Characteristics of the wind drift layer and microscale  
738 breaking waves. *J. Fluid Mech.*, **573**, 417–456.
- 739 Sinha, N., A. E. Tejada-Martinez, C. Akan, and C. E. Grosch, 2015: Toward a k-profile parameter-  
740 ization of langmuir turbulence in shallow coastal shelves. *J. Phys. Oceanogr.*, **45**, 2869–2895.
- 741 Soloviev, A., and R. Lukas, 2003: Observation of wave-enhanced turbulence in the near-surface  
742 layer of the ocean during toga coare. *Deep-Sea Res.*, **50**, 371–395.

743 Sullivan, P. P., J. C. McWilliams, and W. K. Melville, 2004: The oceanic boundary layer driven by  
744 wave breaking with stochastic variability. part 1. direct numerical simulations. *J. Fluid Mech.*,  
745 **507**, 143–174.

746 Teixeira, M. A. C., 2011a: A linear model for the structure of turbulence beneath surface water  
747 waves. *Ocean Modell.*, **36**, 149–162.

748 Teixeira, M. A. C., 2011b: On the connection between dissipation enhancement in the ocean  
749 surface layer and langmuir circulations. *J. Phys. Oceanogr.*, **41**, 2000–2007.

750 Teixeira, M. A. C., 2012: The influence of langmuir turbulence on the scaling for the dissipation  
751 rate in the oceanic boundary layer. *J. Geophys. Res.*, **117**, C05 015.

752 Teixeira, M. A. C., and S. E. Belcher, 2002: On the distortion of turbulence by a progressive  
753 surface wave. *J. Fluid Mech.*, **458**, 229–267.

754 Teixeira, M. A. C., and S. E. Belcher, 2010: On the structure of langmuir turbulence. *Ocean*  
755 *Modell.*, **31**, 105–119.

756 Tejada-Martinez, A. E., C. Akan, C. E. G. N. Sinha, and G. Martinat, 2013: Surface dynamics in  
757 les of full-depth langmuir circulation in shallow water. *Phys. Scr.*, **T155**, 014 008.

758 Terray, E. A., M. A. Donelan, Y. C. Agrawal, W. M. Drennan, K. K. Kahma, A. J. W. III, P. A.  
759 Hwang, and S. A. Kitaigorodskii, 1996: Estimates of kinetic energy dissipation under breaking  
760 waves. *J. Phys. Oceanogr.*, **26**.

761 Terray, E. A., W. M. Drennan, and M. A. Donelan, 1999: The vertical structure of shear and  
762 dissipation in the ocean surface layer. *Proc. Synp. on the Wind-driven Air-Sea Interface-*  
763 *Electromagnetic and Acoustic Sensing, Wave Dynamics and Turbulent Fluxes*, Sydney, Aus-  
764 tralia, University of New South Waves, 239–245.

765 Thorpe, S. A., 2005: *The turbulent ocean*. Cambridge University Press, 439 pp.

766 Van Roekel, L. P., B. Fox-Kemper, P. P. Sullivan, P. E. Hamlington, and S. R. Haney, 2012: The  
767 form and orientation of langmuir cells for misaligned winds and waves. *J. Geophys. Res.*, **117**,  
768 C05 001.



769 **LIST OF TABLES**

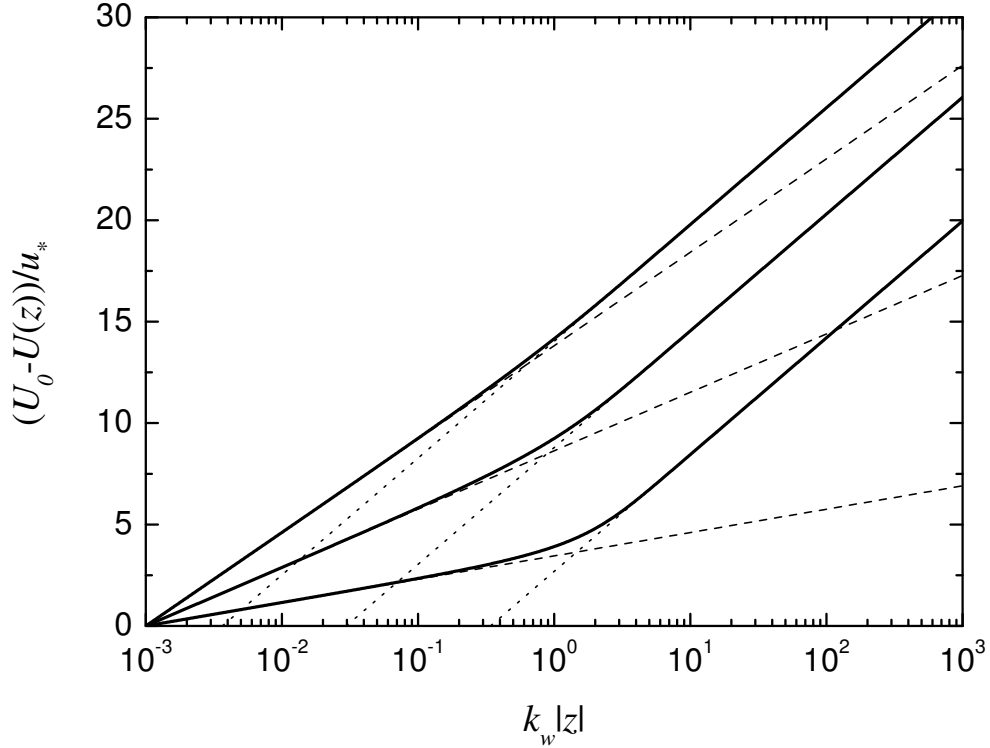
770 **Table 1.** Parameters of the datasets from Cheung and Street (1988) used here, and de-  
 771 rived parameters: wind speed, depth of the boundary layer  $\delta$ , wavelength of the  
 772 dominant waves  $\lambda_w$ , depth of penetration of the wave stress  $1/(\epsilon k_w)$ , surface  
 773 Stokes drift velocity  $U_S(z=0)$ , and turbulent Langmuir number  $La_t$ .  $1/(\epsilon k_w)$ ,  
 774  $U_S(z=0)$  and  $La_t$  were estimated from the dominant wave parameters using  
 775 a monochromatic wave approximation (see text).  $1/(\epsilon k_w)$  is estimated for the  
 776 cases displayed in Figs. 4b and 5a, where  $\epsilon = 0.5$  (the lowest value of  $\epsilon$  con-  
 777 sidered). For other cases,  $\epsilon$  must be changed accordingly. . . . . 37

778 TABLE 1. Parameters of the datasets from Cheung and Street (1988) used here, and derived parameters: wind  
779 speed, depth of the boundary layer  $\delta$ , wavelength of the dominant waves  $\lambda_w$ , depth of penetration of the wave  
780 stress  $1/(\epsilon k_w)$ , surface Stokes drift velocity  $U_S(z=0)$ , and turbulent Langmuir number  $La_t$ .  $1/(\epsilon k_w)$ ,  $U_S(z=0)$   
781 and  $La_t$  were estimated from the dominant wave parameters using a monochromatic wave approximation (see  
782 text).  $1/(\epsilon k_w)$  is estimated for the cases displayed in Figs. 4b and 5a, where  $\epsilon = 0.5$  (the lowest value of  $\epsilon$   
783 considered). For other cases,  $\epsilon$  must be changed accordingly.

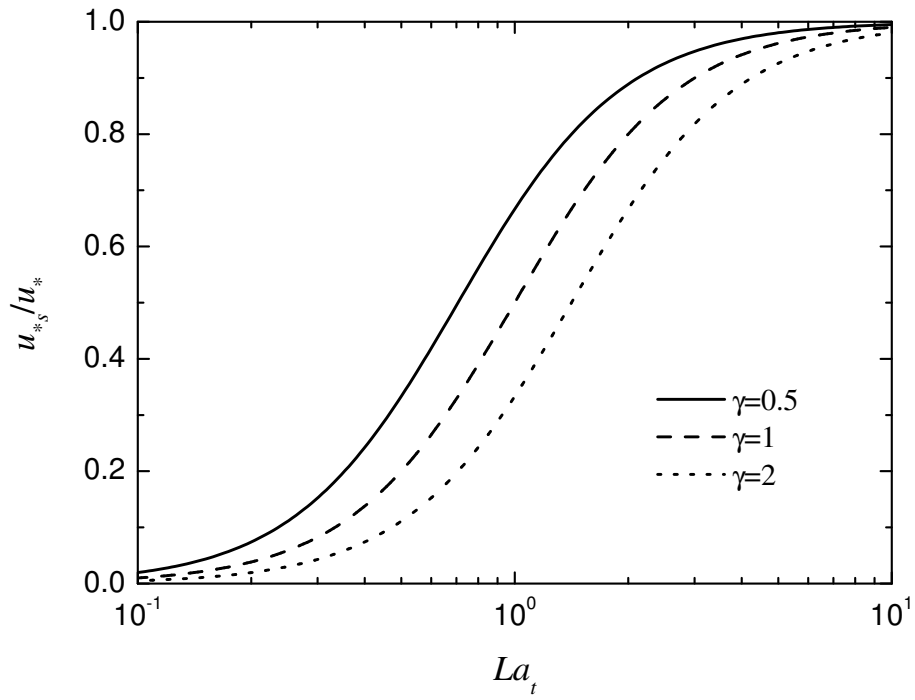
Windspeed ( $\text{ms}^{-1}$ )	$\delta$ (cm)	$\lambda_w$ (cm)	$1/(\epsilon k_w)(\epsilon = 0.5)$ (cm)	$U_S(z=0)$ ( $\text{cms}^{-1}$ )	$La_t$
2.6	31.0	4.2	1.3	0.015	4.7
3.2	34.8	5.8	1.8	0.98	0.71
4.7	26.4	12.7	4.1	2.6	0.52
6.7	24.9	21.4	6.8	4.1	0.53
9.9	35.4	27.1	8.6	6.0	0.54
13.1	29.8	39.0	12.4	9.7	0.53

## LIST OF FIGURES

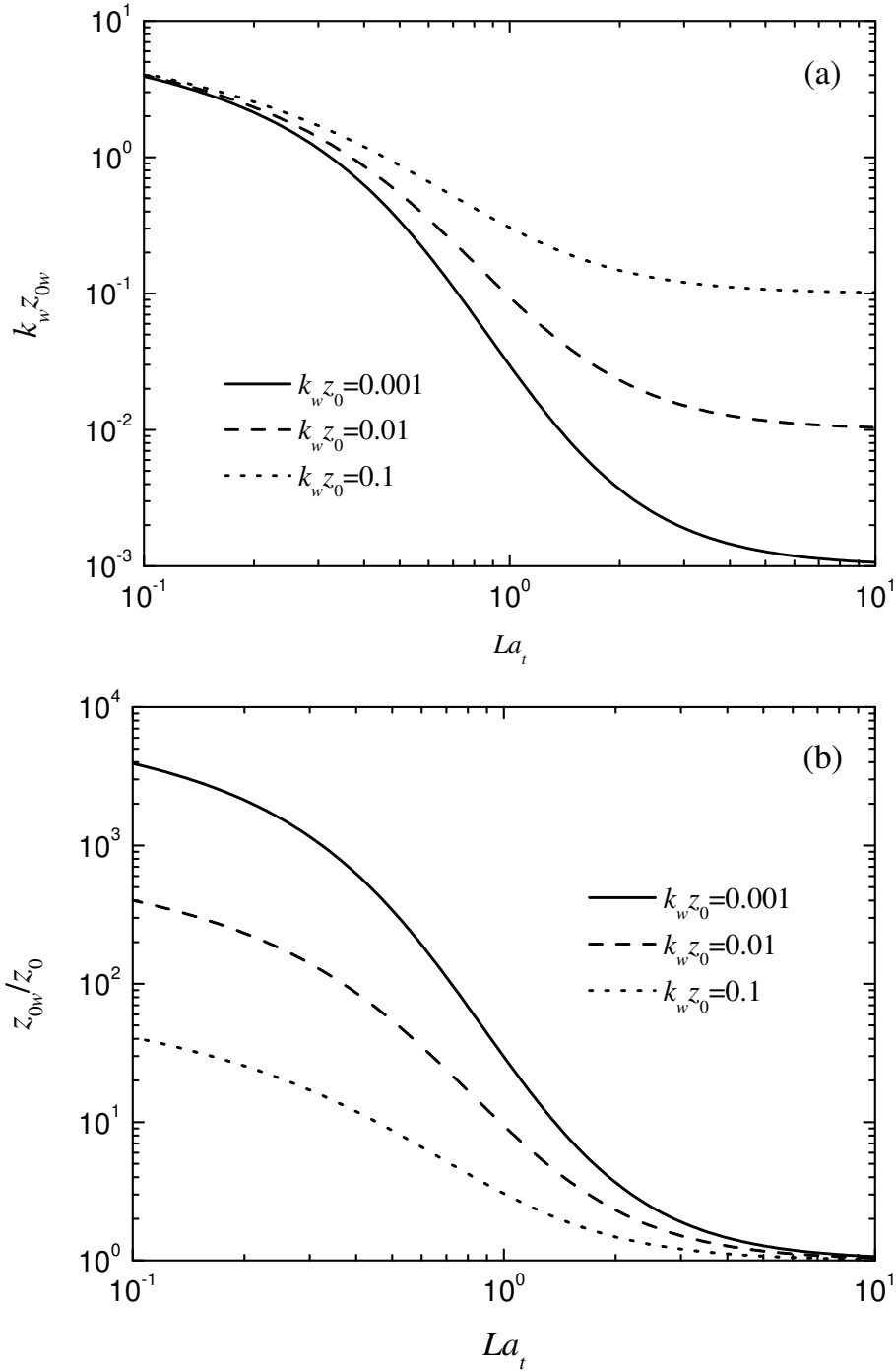
785	<b>Fig. 1.</b>	Normalized current speed as a function of normalized depth for different values of $La_t$ , calculated from (15) for $\gamma = 1$ , $\varepsilon = 1$ and $k_w z_0 = 0.001$ . Solid lines: current profiles, for $La_t = 2$ , $La_t = 1$ and $La_t = 0.5$ (from top to bottom). Dashed lines: extension of the asymptotes (with slope $(u_{*s}/u_*)/\kappa$ ) corresponding to the currents at small depths to large depths. Dotted lines: extension of the asymptotes (with slope $1/\kappa$ ) corresponding to the currents at large depths up to the depths where the currents would be zero, corresponding to the values of the apparent roughness length $k_w z_{0w}$ . . . . .	39
792	<b>Fig. 2.</b>	Ratio of the shear-associated friction velocity to the total friction velocity as a function of $La_t$ for different values of $\gamma$ , calculated from (9). See legend for meaning of different line types. . . . .	40
795	<b>Fig. 3.</b>	Normalized apparent roughness length as a function of $La_t$ for $\gamma = 1$ and $\varepsilon = 1$ from (21), for different values of $k_w z_0$ . (a) Apparent roughness length normalized by $k_w$ , (b) ratio of apparent to true roughness length. See legend for meaning of different line types. . . . .	41
798	<b>Fig. 4.</b>	Comparison between normalized current speed profiles in wall-coordinates from the model developed here, given by (16) or (17) (lines), and from the measurements of Cheung and Street (1988) (symbols), for different wind speeds. The model assumes $c_1 = 0.11$ and $c_2 = 0$ in (26). Solid line and filled circles: $2.6 \text{ m s}^{-1}$ , dashed line and squares: $3.2 \text{ m s}^{-1}$ , dotted line and triangles: $4.7 \text{ m s}^{-1}$ , dash-dotted line and diamonds: $6.7 \text{ m s}^{-1}$ , dash-double-dotted line and stars: $9.9 \text{ m s}^{-1}$ , short-dotted line and open circles: $13.1 \text{ m s}^{-1}$ . (a) $\gamma = 2$ and $\varepsilon = 2$ , (b) $\gamma = 0.5$ and $\varepsilon = 0.5$ . . . . .	42
805	<b>Fig. 5.</b>	Similar to Fig. 4, but for $c_1 = 0.2$ and $c_2 = 0.9$ in (26), and different values of $\gamma$ and $\varepsilon$ . (a) $\gamma = 0.25$ and $\varepsilon = 0.5$ , (b) $\gamma = 0$ (i.e., no wave effects). . . . .	43
807	<b>Fig. 6.</b>	Similar to Fig. 5, but using the finite-depth model for which the shear stress decreases linearly with depth (24), with $\gamma = 0.25$ , $\varepsilon = 1$ , $c_1 = 0.2$ and $c_2 = 0.9$ . The vertical lines (same type as the corresponding current profiles) denote the depths at which the shear stress reaches zero in each case ( $z^+ = \delta u_*/\nu$ ). Note that the current profiles for larger depths remain constant in the model . . . . .	44
812	<b>Fig. 7.</b>	Normalized current speed at the surface predicted by the finite-depth model (24) (for $z^+ = \delta u_*/\nu$ ) as a function of corresponding values derived from the measurements. Circles: measured values taken directly from Table 1 of Cheung and Street (1988), triangles: measured values taken as the data point at the largest depth from the datasets corresponding to each different wind speed. . . . .	45



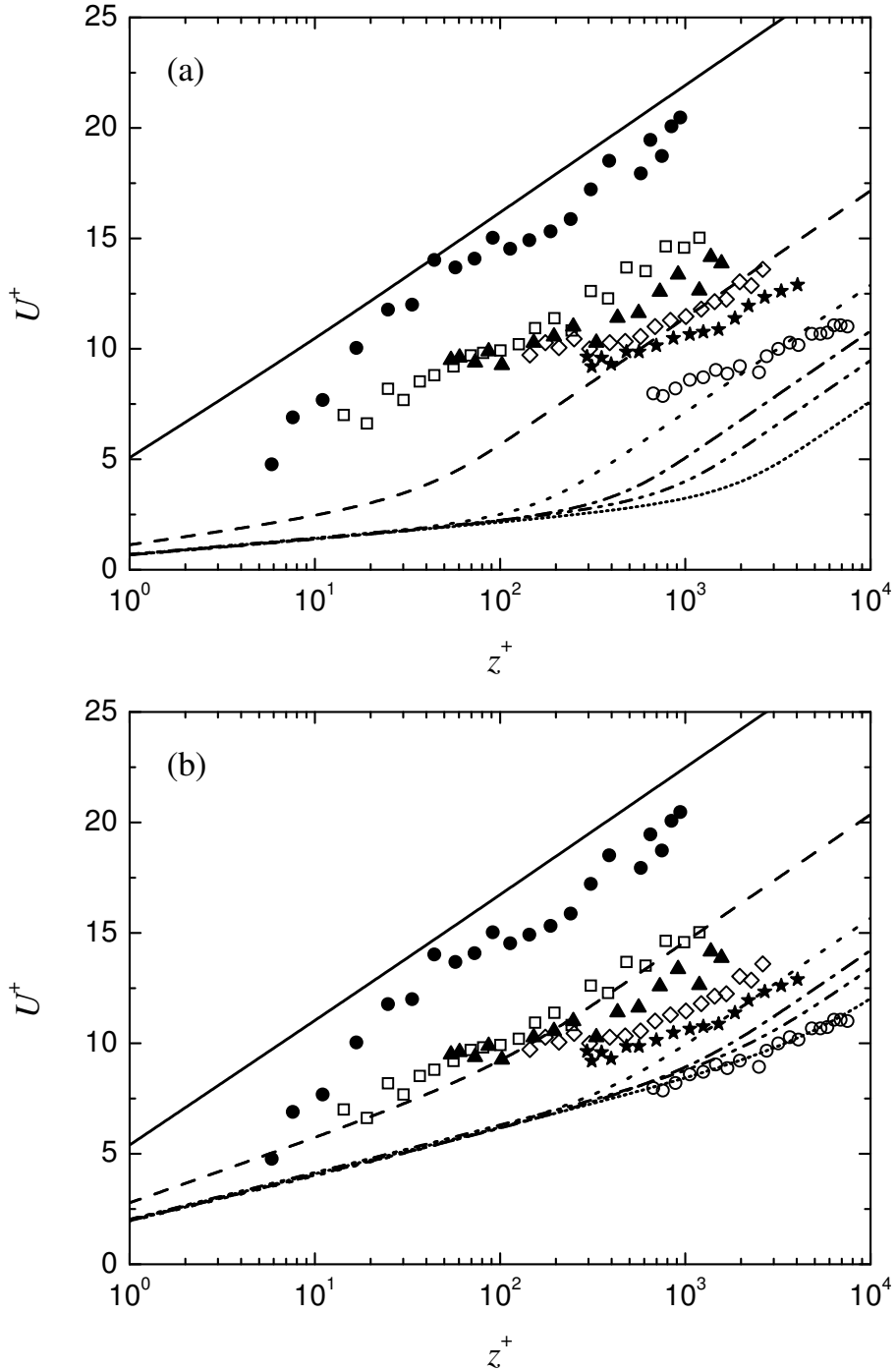
817 FIG. 1. Normalized current speed as a function of normalized depth for different values of  $La_t$ , calculated from  
 818 (15) for  $\gamma = 1$ ,  $\varepsilon = 1$  and  $k_w z_0 = 0.001$ . Solid lines: current profiles, for  $La_t = 2$ ,  $La_t = 1$  and  $La_t = 0.5$  (from  
 819 top to bottom). Dashed lines: extension of the asymptotes (with slope  $(u_{*s}/u_*)/\kappa$ ) corresponding to the currents  
 820 at small depths to large depths. Dotted lines: extension of the asymptotes (with slope  $1/\kappa$ ) corresponding to the  
 821 currents at large depths up to the depths where the currents would be zero, corresponding to the values of the  
 822 apparent roughness length  $k_w z_{0w}$ .



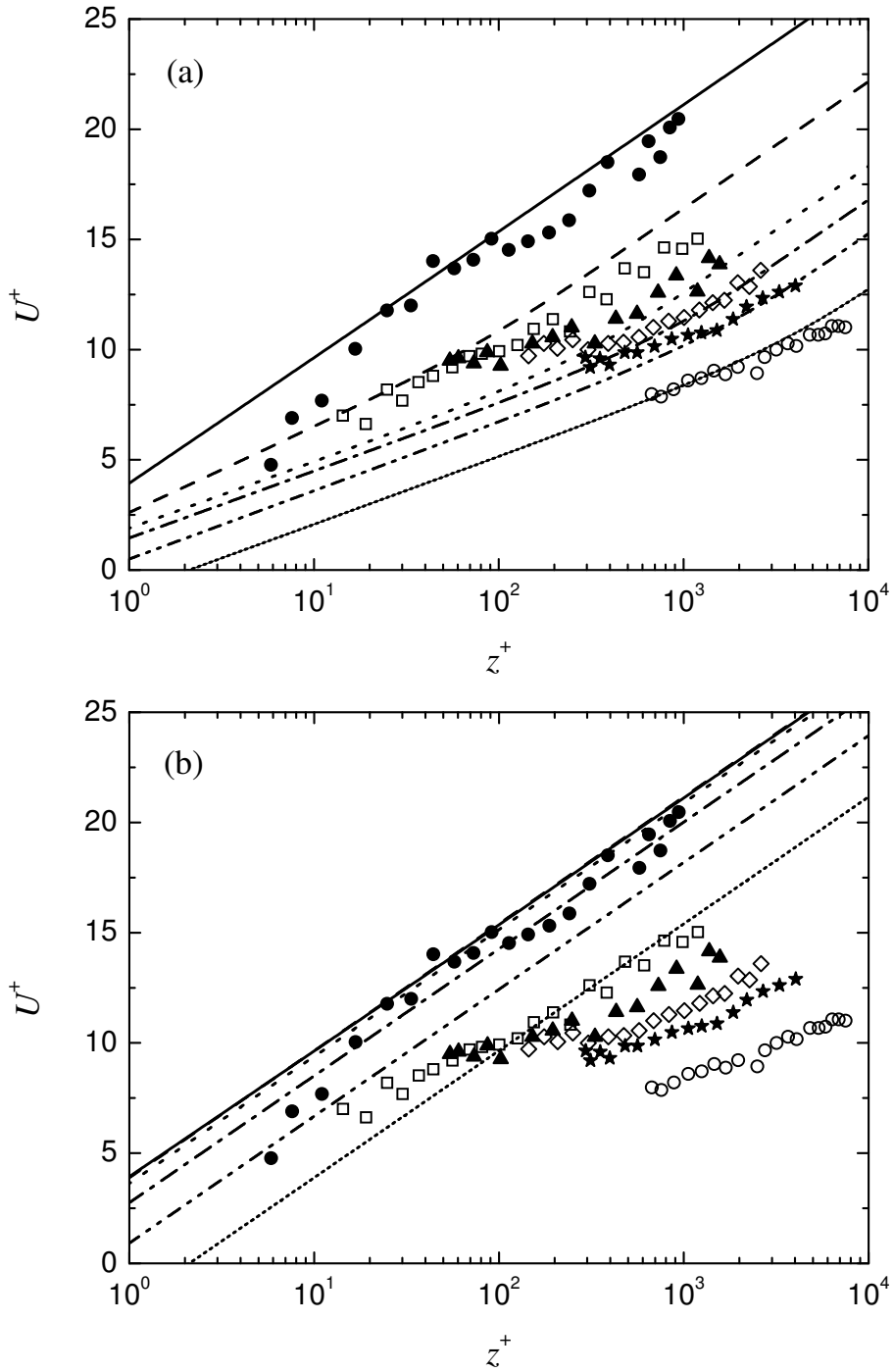
823 FIG. 2. Ratio of the shear-associated friction velocity to the total friction velocity as a function of  $La_t$  for  
 824 different values of  $\gamma$ , calculated from (9). See legend for meaning of different line types.



825 FIG. 3. Normalized apparent roughness length as a function of  $La_t$  for  $\gamma = 1$  and  $\varepsilon = 1$  from (21), for different  
 826 values of  $k_w z_0$ . (a) Apparent roughness length normalized by  $k_w$ , (b) ratio of apparent to true roughness length.  
 827 See legend for meaning of different line types.

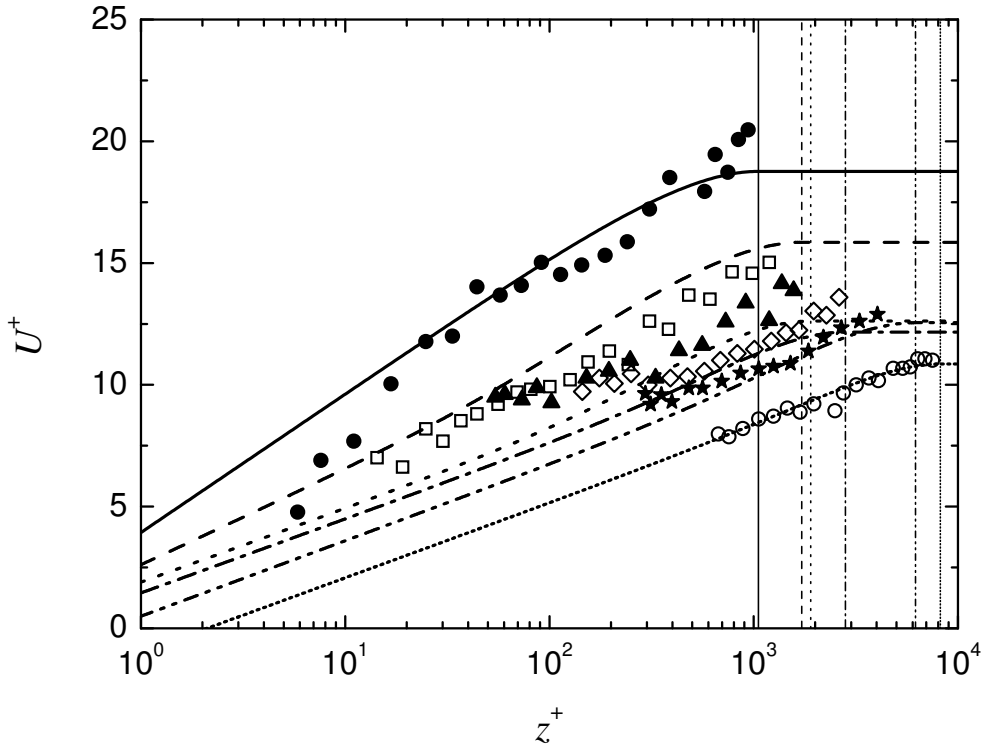


828 FIG. 4. Comparison between normalized current speed profiles in wall-coordinates from the model developed  
 829 here, given by (16) or (17) (lines), and from the measurements of Cheung and Street (1988) (symbols), for differ-  
 830 ent wind speeds. The model assumes  $c_1 = 0.11$  and  $c_2 = 0$  in (26). Solid line and filled circles:  $2.6 \text{ m s}^{-1}$ , dashed  
 831 line and squares:  $3.2 \text{ m s}^{-1}$ , dotted line and triangles:  $4.7 \text{ m s}^{-1}$ , dash-dotted line and diamonds:  $6.7 \text{ m s}^{-1}$ , dash-  
 832 double-dotted line and stars:  $9.9 \text{ m s}^{-1}$ , short-dotted line and open circles:  $13.1 \text{ m s}^{-1}$ . (a)  $\gamma = 2$  and  $\varepsilon = 2$ , (b)  
 833  $\gamma = 0.5$  and  $\varepsilon = 0.5$ .

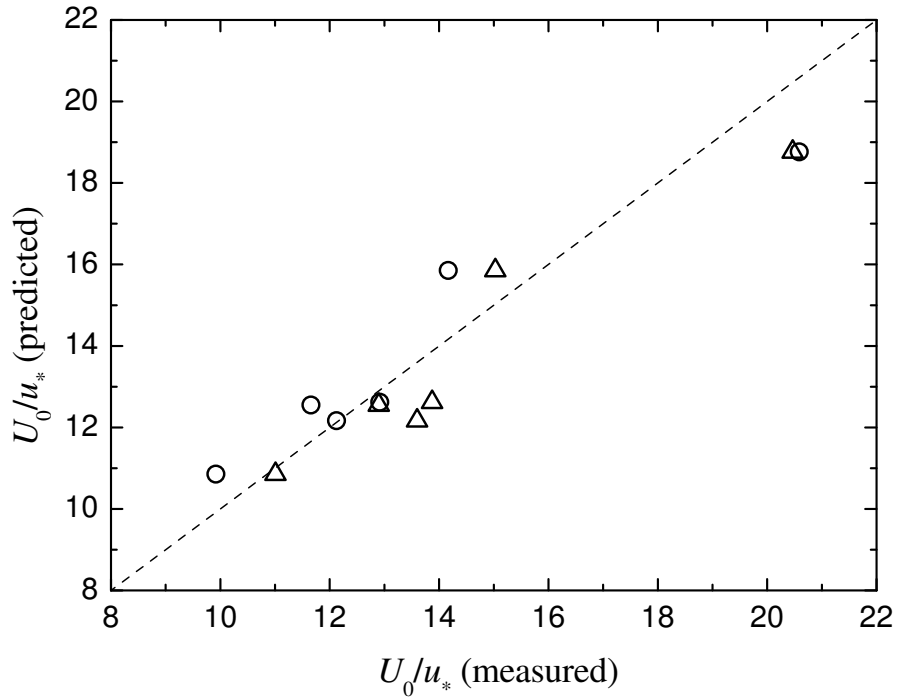


834 FIG. 5. Similar to Fig. 4, but for  $c_1 = 0.2$  and  $c_2 = 0.9$  in (26), and different values of  $\gamma$  and  $\varepsilon$ . (a)  $\gamma = 0.25$   
 835 and  $\varepsilon = 0.5$ , (b)  $\gamma = 0$  (i.e., no wave effects).





836 FIG. 6. Similar to Fig. 5, but using the finite-depth model for which the shear stress decreases linearly with  
 837 depth (24), with  $\gamma = 0.25$ ,  $\varepsilon = 1$ ,  $c_1 = 0.2$  and  $c_2 = 0.9$ . The vertical lines (same type as the corresponding  
 838 current profiles) denote the depths at which the shear stress reaches zero in each case ( $z^+ = \delta u_* / \nu$ ). Note that  
 839 the current profiles for larger depths remain constant in the model



840 FIG. 7. Normalized current speed at the surface predicted by the finite-depth model (24) (for  $z^+ = \delta u_*/\nu$ )  
 841 as a function of corresponding values derived from the measurements. Circles: measured values taken directly  
 842 from Table 1 of Cheung and Street (1988), triangles: measured values taken as the data point at the largest depth  
 843 from the datasets corresponding to each different wind speed.